

Review

Luminescent Lifetime Regulation of Lanthanide-Doped Nanoparticles for Biosensing

Mingkai Wang ^{1,2}, Chuanyu Hu ^{1,*} and Qianqian Su ^{2,*} 

¹ Department of Stomatology, Tongji Hospital, Tongji Medical College, Huazhong University of Science and Technology, Wuhan 430074, China; wmk19961108@163.com

² Institute of Nanochemistry and Nanobiology, Shanghai University, Shanghai 200444, China

* Correspondence: chuanyuhu@hust.edu.cn (C.H.); chmsqq@shu.edu.cn (Q.S.)

Abstract: Lanthanide-doped nanoparticles possess numerous advantages including tunable luminescence emission, narrow peak width and excellent optical and thermal stability, especially concerning the long lifetime from microseconds to milliseconds. Differing from other shorter-lifetime fluorescent nanomaterials, the long lifetime of lanthanide-doped nanomaterials is independent with background fluorescence interference and biological tissue depth. This review presents the recent advances in approaches to regulating the lifetime and applications of bioimaging and biodetection. We begin with the introduction of the strategies for regulating the lifetime by modulating the core-shell structure, adjusting the concentration of sensitizer and emitter, changing energy transfer channel, establishing a fluorescence resonance energy transfer pathway and changing temperature. We then summarize the applications of these nanoparticles in biosensing, including ion and molecule detecting, DNA and protease detection, cell labeling, organ imaging and thermal and pH sensing. Finally, the prospects and challenges of the lanthanide lifetime regulation for fundamental research and practical applications are also discussed.

Keywords: luminescence lifetime; lanthanide-doped nanoparticles; lifetime regulation; bioimaging; biodetection; biosensing



Citation: Wang, M.; Hu, C.; Su, Q. Luminescent Lifetime Regulation of Lanthanide-Doped Nanoparticles for Biosensing. *Biosensors* **2022**, *12*, 131. <https://doi.org/10.3390/bios12020131>

Received: 11 January 2022

Accepted: 12 February 2022

Published: 19 February 2022

Publisher's Note: MDPI stays neutral with regard to jurisdictional claims in published maps and institutional affiliations.



Copyright: © 2022 by the authors. Licensee MDPI, Basel, Switzerland. This article is an open access article distributed under the terms and conditions of the Creative Commons Attribution (CC BY) license (<https://creativecommons.org/licenses/by/4.0/>).

1. Introduction

A central goal in biology and medicine is to develop excellent imaging and detection technology [1]. Researchers have devoted massive efforts to developing fluorescence imaging technology through fluorescent nanomaterials, including quantum dots (QDs) [2], upconversion nanomaterials (UCNPs) [3], carbon-based nanomaterials [4], stoichiometric metal oxides [5], perovskite [6], metal nanomaterials [7] and other materials [8]. In addition, biological images were obtained in a non-invasive manner under laser excitation [9], which has great labeling ability, high signal strength, fast imaging speed and a wide range of applications [10–13]. However, there are numerous limitations based on conventional fluorescence imaging technology, including low sensitivity, shallow detective depth and substantial interference caused by background autofluorescence [14,15]. Among the large number of nanomaterials, lanthanide-doped nanoparticles feature a longer lifetime than other fluorescence materials, whose emission could last for milliseconds [16]. Based on these nanoparticles, lifetime imaging and detection platform were proposed to resolve the difficulty of conventional fluorescence imaging [17,18].

Unsusceptible to the concentration of nanoparticles [19], laser intensity [20] and biological tissue thickness [21], the quality of luminescence lifetime imaging is better than traditional luminescence imaging in the cell or tissue microenvironment [22]. Moreover, the sensitivity of time-gated imaging with an optical chopper offers more than one order of magnitude than that of the traditional method using optical band-pass filters [23]. The luminescence lifetime of lanthanides depends on their intrinsic properties and the localized

microenvironment, involving pH value, doped ion concentration, protein interaction and other factors affecting the decay process [24]. Therefore, lifetime encoding was achieved by nanostructural engineering, while lifetime sensing was produced by changing the relying circumstances. Correspondingly, the time-resolved technology was developed rapidly due to its unique properties [25].

In this review, we focus on the recent advances in the regulating lifetime of lanthanide for biosensing and imaging (Figure 1). In Section 1, we introduce the strategies of lifetime modulation for lanthanide-doped nanoparticles, involving core–shell structure design, concentration adjusting, energy transfer channel controlling and temperature controlling. In Section 2, we discuss the use of the probes for ions and molecules, DNA and protease sensing, cell labeling, organ imaging and thermal and pH sensing. Finally, we discuss the prospects and challenges for possible development directions and application scenarios.

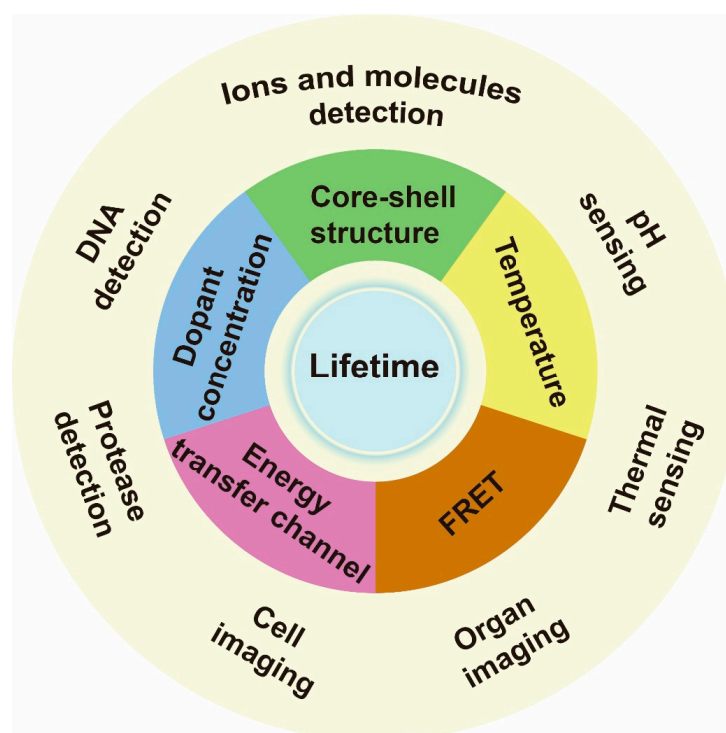


Figure 1. Schematic illustrations of lanthanide-doped nanoparticle lifetime regulation for biosensing. The approaches to regulating lifetime include varying core–shell structure, dopant concentration, energy transfer channel, temperature and setting a fluorescence resonance energy transfer (FRET) system. The relevant applications include ions, molecules, DNA, protease, thermal and pH sensing, as well as cell labeling and organ imaging.

2. Lifetime Regulation

Luminescence lifetime refers to the average time the molecule spends in the excited state returning to the ground state [26]. The lifetime of a phosphor, τ , refers to the time at which the intensity decays to $1/e$ of its maximum [27]. The decay of one emitting state in an upconversion energy transfer process is determined by its intrinsic decay and the intermediate states [28]. Susceptible to their intrinsic properties and local environment, the lifetime of lanthanide-doped nanoparticles could be tuned by adjusting core–shell structure, the content of sensitizer and emitter, internal energy transfer channel, FRET system and temperature. Nanocrystals with a controllable lifetime have been widely used in biosensing to eliminate background autofluorescence and light scattering interference. However, the reported methods allow only a limited range of lifetime adjustments.

2.1. Variation of Core–Shell Structures

Core–shell engineering is generally utilized to reduce surface quenching effects [29]. Shell passivation could promote the upconversion process by promoting the occurrence of energy hopping in higher-lying excited states [30]. Therefore, lifetime is affected by the shell layers, including the shell thickness and shell composition.

2.1.1. Core Size

The defect density of core nanoparticles doped with sensitizers and emitters decreases as the nanoparticle's size increases. Jin et al. found an increase in the lifetime of Yb, Er-doped UCNPs with the increase of their size by comparing the lifetime of these nanoparticles ranging from 6 nm to 45 nm (Figure 2a). With the assistance of a mathematical model, it was verified that the decay time was related to surface-to-volume ratio and shell thickness. In addition, the lifetime of β -phase particles has significant relationships with surface defect, solvent and vibration energy of surface ligands, while defect density only matters for α -phase nanocrystals [31]. Liu et al. compared the decay curves of different sizes of NaYF₄: 20%Yb,2%Er ranging from 15.3 nm to 27.2 nm, exhibiting the increase in the lifetime of both Er³⁺ and Yb³⁺ at 540 nm and 985 nm, respectively, as the nanoparticle dimension expanded [32].

2.1.2. Inert Shell Passivation

The epitaxial shell could protect the excitation energy from trapping by surface ligands or solvent molecules, leading to a long-lived lifetime. Su et al. designed a core–shell–shell heterostructure to prolong the lifetime of upconversion emitters. An optically inert NaYF₄ shell on the surface of NaGdF₄@NaGdF₄ core–shell nanoparticle could efficiently block the energy transfer from Gd³⁺ to surface quenchers, thereby promoting efficient upconversion emission and long lifetimes of Gd³⁺ [33]. Mao et al. successively compared the decay curves of NaYF₄: Yb/Er/Mn (C_d), NaYF₄@NaYF₄: Yb/Er/Mn (C/S_d), NaYF₄: Yb/Er/Mn@NaYF₄ (C_d/S) and NaYF₄@NaYF₄: Yb/Er/Mn@NaYF₄ (C/S_d/S), finding the lifetime became longer. Amongst them, the C/S_d/S structure has two layers of NaYF₄ interface contacting the active shell, which reduced surface defects and thus enhanced the upconversion process. Therefore, the lifetime can be prolonged by reducing energy defects and increasing the energy transfer rate [34].

CaF₂ is a biocompatible and fluoride-rich matrix that is well used as a shell in upconversion nanomaterials, which can simultaneously suppress the interfacial diffusion of Ln³⁺ and surface quenching [35]. After heterogenous CaF₂ layer was coated on the NaGdF₄: Yb,Er, the lifetime of Er³⁺ at 532 nm prolonged from 89 μ s to 162 μ s, accompanied by the green (²H_{11/2}, ⁴S_{3/2} → ⁴I_{15/2}) and red (⁴I_{15/2} → ⁴I_{15/2}) emissions of Er³⁺ enhanced 24.2 and 55.5 times, respectively [36]. When CaF₂ grew on the core of NaYF₄: 10%Yb,30%Nd, the lifetime of Yb³⁺ at 1000 nm increased from 51 μ s up to 833 μ s, indicating the surface lattice defects were minimized [37].

Interestingly, Su et al. provided an upconverted excitation lock-in (UCEL) mode to block the energy consumption of Gd³⁺ caused by lattice defects and impurities. NaYF₄-based interlayer can effectively suppress the energy loss within the nanoparticles induced by inner lattice defects and promote energy recycling in the core domain. Therefore, the lifetime and the emission intensity of the heterogeneous structure significantly increased compared with the homogeneous counterparts (Figure 2b) [38].

Increasing shell thickness could suppress the non-radiative effect and cross-relaxation. Liu et al. synthesized NaYF₄: Yb³⁺,Er³⁺@mNaYF₄ (m = 0, 1, 2, 3, 4, 5) core–shell nanoparticles with different shell thicknesses (7.5 nm, 9 nm, 10 nm, 11 nm, 11.8 nm and 16.5 nm). The corresponding lifetimes of these nanoparticles were measured to be 10.10 μ s, 11.57 μ s, 15.78 μ s, 19.77 μ s, 23.51 μ s and 26.52 μ s due to the protection of shell [39]. Furthermore, increasing heterogenous shell thickness could minimize surface quenching. Coating a CaF₂ shell with a range of thickness from 0 nm to 5.3 nm on the NaYbF₄, the lifetime of Yb³⁺ of 980 nm increased from 33 μ s to 2.18 ms, excited at 920 nm measured by an optical

parametric oscillator (OPO) laser. Therein, when the CaF_2 shell thickness reached 2.6 nm, the luminescence lifetime value was approximate to the radiative lifetime of Yb^{3+} [40].

2.1.3. Active Shell

With regard to the active shell, Liu et al. proved that increasing the concentration of sensitizer in the shell had adverse impacts on the luminescence intensity and lifetime enhancement. In a $\text{NaYF}_4: 20\% \text{Yb}, 2\% \text{Er} @ \text{NaYF}_4: m\% \text{Yb}$ ($m = 0, 10, 20$) nanoparticle, the lifetime of Er^{3+} and Yb^{3+} at 540 nm and 985 nm decreased when the concentration of Yb^{3+} in the shell increased. This can be attributed to the fact that more sensitizers in the shell increased the possibility of energy trapped by the surface defect. In addition, a lower energy transfer efficiency was observed due to the longer distance between sensitizer and emitter compared with that in the counterpart consisting of inner sensitizers [32].

A longer migration distance imparted by thicker energy migration layers or an increased number of migration steps may prolong luminescence lifetime. In a core/multishell $\text{NaYF}_4 @ \text{NaYbF}_4 @ \text{NaYF}_4: \text{Yb}^{3+} / \text{Tm}^{3+} @ \text{NaYF}_4$ nanoparticle, the thickness of the energy migration layer (NaYbF_4) increased from 0, 1.5, 3.0, 5.0 to 8.0 nm gradually, and the lifetime at 808 nm increased from 867, 1027, 1162, 1201 to 1282 μs , respectively [41]. When the thickness of the shell doped with sensitizers (i.e., Yb^{3+}) increased, the lifetime of activators was longer in the core due to Yb energy migration. Increasing the thickness of the second layer in the $\beta\text{-NaGdF}_4: 25\% \text{Yb}, 1\% \text{Tm} @ \text{NaYF}_4: 10\% \text{Yb} @ \text{NaNdF}_4: 10\% \text{Yb} @ \text{NaYF}_4$ from 1.5 nm to 5.4 nm, the lifetime at 475 nm prolonged from 632 μs to 836 μs [42]. In addition, with $\text{NaGdF}_4 @ \text{NaGdF}_4: \text{Yb}, \text{Er} @ \text{NaYF}_4: \text{Yb} @ \text{NaNdF}_4: \text{Yb}$ used as an experimental model, the lifetime at 1525 nm was enhanced when increasing the thickness of the energy relay layer ($\text{NaYF}_4: \text{Yb}$), which was attributed to the enlarged distance from sensitizers to emitters. A similar trend was also observed in Ho^{3+} -doped nanoparticles (Figure 2c). Meanwhile, a certain Yb^{3+} -doped shell thickness corresponded to the determined capacity of Yb^{3+} sublattice. Therefore, increasing the concentration of emitters could accelerate the stored energy into luminescence emission, resulting in a shortened lifetime. As the proportion of Er^{3+} rose from 0.5% up to 32%, the lifetime at 540 nm decreased from 101 μs to 13 μs [43].

2.2. Changing Concentration of Sensitizer and Emitter

Excessive emitters would increase the probability of cross-relaxation, leading to concentration quenching. For a $\text{Yb}^{3+}\text{-Er}^{3+}\text{-Ho}^{3+}$ tri-doped nanoparticle, higher content of Ho^{3+} could shorten the interionic distances of $\text{Yb}^{3+}\text{-Er}^{3+} / \text{Ho}^{3+}$, $\text{Er}^{3+}\text{-Ho}^{3+}$ and $\text{Ho}^{3+}\text{-Ho}^{3+}$, which could enhance the non-radiative process and energy transfer (ET) sensitization. A decrease in the lifetime of Ho^{3+} (643 nm, 750 nm, 895 nm), Er^{3+} (525 nm, 545 nm, 655 nm, 810 nm, 845 nm) and Yb^{3+} (1020 nm) was observed when increasing the concentration of Ho^{3+} [44]. Similarly, as the mole content of Tm^{3+} rose from 0.2% to 8% in $\text{NaYF}_4: 20\% \text{Yb}, x\% \text{Tm}$ (40 nm), the lifetime of the blue emission was reduced from 662.4 μs to 25.6 μs (Figure 3a). Meanwhile, as the mole percentage of Yb^{3+} rose from 10% to 30% in $\text{NaYF}_4: x\% \text{Yb}, 1\% \text{Tm}$, the lifetime of the same blue emission decreased from 206.7 μs to 120.2 μs [20]. The higher concentration of part of emitters would likely cause self-aggregation and cross relaxation, resulting in a shortened lifetime. When the Er^{3+} concentration was varying from 1% to 70% in the $\beta\text{-NaYbF}_4 @ \text{NaY}_{0.8-x}\text{Er}_x\text{Gd}_{0.2}\text{F}_4 @ \text{NaY}_{0.8}\text{Gd}_{0.2}\text{F}_4$, the lifetime of Er^{3+} at the level of $^4\text{S}_{3/2}$ (540 nm) decreased sequentially. The shorter lifetime was attributed to the noneffective passivation on the surface when dopant with a higher concentration of emitters. Due to the greater energy from Yb^{3+} ($^2\text{F}_{5/2}$) being transferred to Er^{3+} ($^4\text{S}_{3/2}$, $^4\text{S}_{9/2}$), the lifetime of Yb^{3+} was shortened. With the lack of cross-relaxation pathways for the $^4\text{S}_{9/2}$ level of Er^{3+} , the lifetime rarely has significant changes with the Er^{3+} concentration variation. Interestingly, the lifetime of Er^{3+} at 654 nm in the $\beta\text{-NaYbF}_4 @ \text{NaY}_{0.8-x}\text{Er}_x\text{Gd}_{0.2}\text{F}_4$ structure had a long lifetime due to more incredible energy transferring to the surface [45].

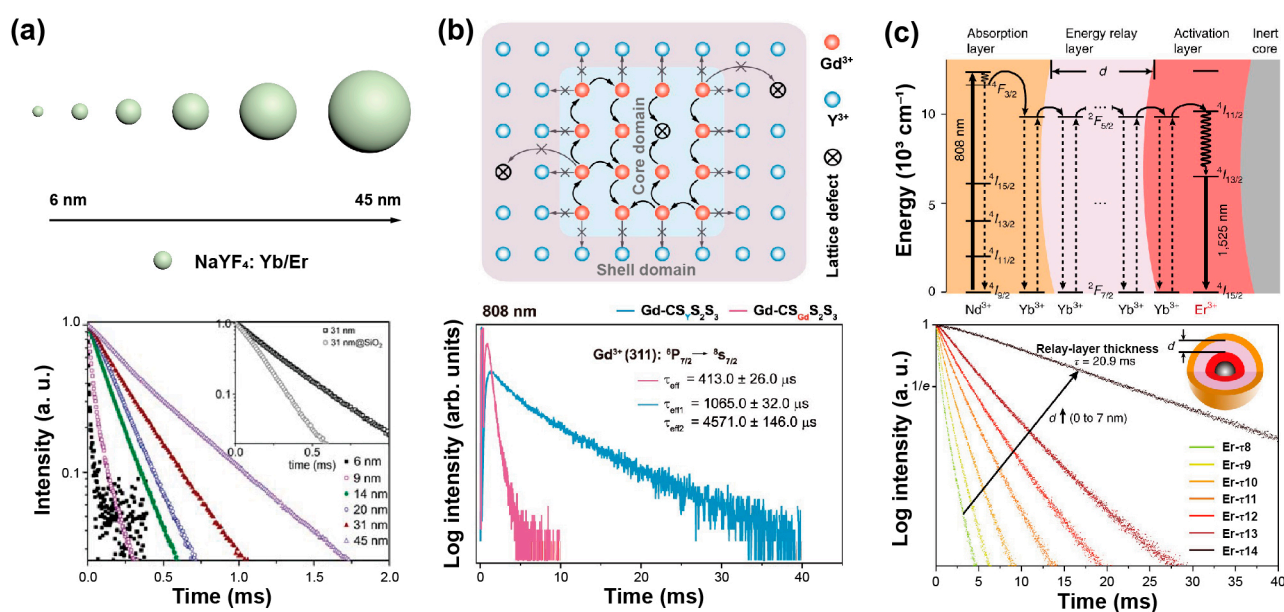


Figure 2. (a) The schematic description for the size of NaYF₄: Yb,Er nanoparticles and lifetime decay curves of green emission in these nanoparticles. Reproduced with permission from [31]. Copyright 2013, Royal Society of Chemistry. (b) The diagram of energy transfer mechanism in NaGdF₄: 49%Yb,1%Tm coated with heterogeneous shell nanoparticle, and corresponding lifetimes of Gd³⁺ in homogeneous and heterogeneous nanoparticles at 310 nm under 808 nm excitation. Reproduced with permission from [38]. Copyright 2021, Nature Publishing Group. (c) The diagrammatic drawing of energy transfer process in the core–multishell nanoparticles and luminescence decay curves at 1525 nm with the energy relay shell thickness ranging from 0 nm to 7 nm. Reproduced with permission from [43]. Copyright 2018, Nature Publishing Group.

Simultaneous excitation of two Yb³⁺ ions can produce Yb³⁺ dimers with higher excitation energy, which could upconvert photons to Tb³⁺. To study the composition-dependent emission lifetimes and the effect on the energy transfer efficiency, Yan et al. employed the Tb³⁺-Yb³⁺-Nd³⁺ co-doped NaGdF₄: 80%Yb,10%Tb@NaGdF₄: 50%Nd,10%Yb nanoparticles with varied doping concentrations as the study model. The lifetime of Tb³⁺ reached 1.76 ms when the content of Yb³⁺ rose from 20% to 80% because more Yb³⁺ facilitated the formation of Yb³⁺ dimer. The lifetime at 542 nm is slightly prolonged by 0.06 ms when the proportion of Tb³⁺ increased from 5% to 10% due to promoted energy transfer from Yb³⁺ dimer to Tb³⁺. In addition, when the content of Nd³⁺ increased from 10% to 50%, near-infrared absorption intensity improved, the lifetime of Tb³⁺ at 542 nm and Yb³⁺ at 1000 nm both increased, indicating more energy was transferred to Tb³⁺ and Yb³⁺ [46].

A constant lifetime can be obtained when the doping content of the sensitizer is changed. To investigate the relationship between lifetime decay behavior and luminescence emission intensity, core–shell structure of NaYF₄@NaYF₄: x%Yb,1%Tm@NaYF₄: y%Yb@NaYF₄ nanoparticles was developed by Zhang et al. Changing the mole content of Yb³⁺ in the first shell from 20% up to 80%, the emissive intensity changed while the luminescence lifetime at 475 nm kept constant, suggesting a constant lifetime with different emissive intensity could be obtained. When the concentration of Yb³⁺ in the first and second shell layers was changed, the varied lifetime (1256 ms to 310 ms) was obtained with a constant emission intensity (Figure 3b) [47]. For the mentioned nanoparticles, the declined Yb³⁺ concentration increased the mean value of the distance between Yb³⁺ and Tm³⁺ ions, leading to a longer lifetime due to the weakened back energy transfer process. The Yb³⁺ concentration in the energy transfer upconversion layers was decreased from 99%, 70%, 50%, 40%, 20% to 10%, resulting in the lifetime at 808 nm being increased from 1282, 1315, 1481, 1618, 1721 to 2157 μs, respectively [41]. Besides, the Tm³⁺ could be served as sensitizers and transfer energy to Yb³⁺, Ho³⁺ and Er³⁺ when excited at 808 nm and

1208 nm, respectively. The lifetime of Yb^{3+} (980 nm), Ho^{3+} (1180 nm) and Er^{3+} (1525 nm) decreased with the increase of the Tm^{3+} molar ratio [48].

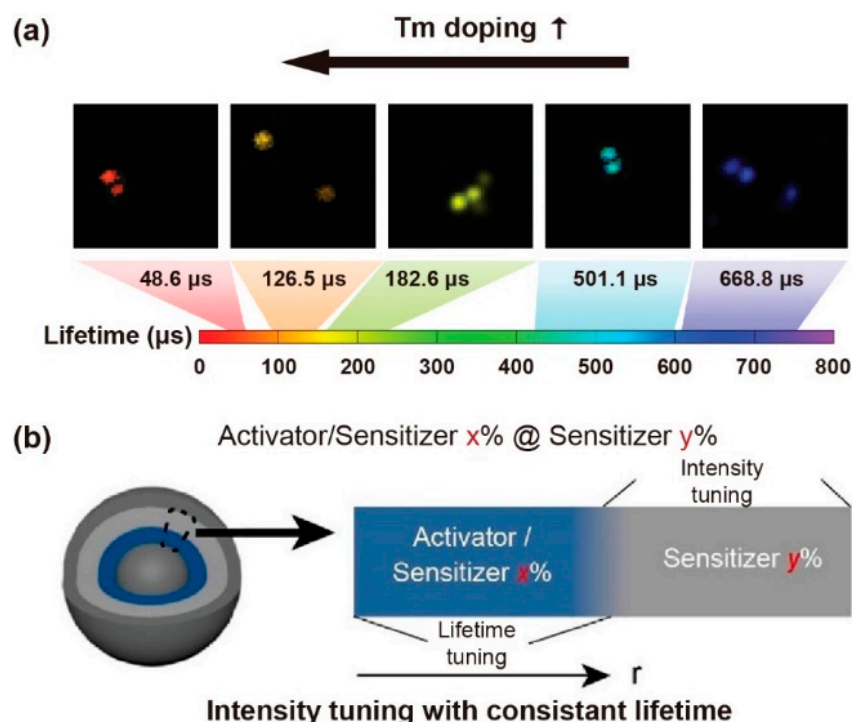


Figure 3. (a) The time-resolved confocal images of $\text{NaYF}_4: \text{Yb}, \text{Tm}$ nanoparticles and the lifetime tuning scheme by changing Tm^{3+} doping concentrations. Reproduced with permission from [20]. Copyright 2014, Nature Publishing Group. (b) Diagrammatic illustration of consistent lifetime with tunable intensity by doping various sensitive gradients in the shell. Reproduced with permission from [47]. Copyright 2021, WILEY-VCH.

2.3. Adjusting the Energy Transfer Channel

The decay process of an excited state is inversely proportional to the energy transfer rate and the radiative and non-radiative transition rates. Tri-doped nanoparticles of $\text{NaYF}_4 @ \text{NaYF}_4: \text{Er}^{3+} / \text{Yb}^{3+} / \text{Mn}^{2+} @ \text{NaYF}_4$ were synthesized by Mao et al., exhibiting the new energy transfer process between Mn^{2+} and Er^{3+} . With a non-radiative energy transfer channel created between the level of Mn^{2+} ($^4\text{T}_1$) and Er^{3+} ($^2\text{H}_{11/2}$ and $^4\text{S}_{3/2}$), the overall transition rate increased owing to the resonance energy transfer, leading to a reduced lifetime of Er^{3+} at 550 nm. The presence of Mn^{2+} ions promoted the relaxation of the $^4\text{S}_{3/2}$ energy level, and the red emission of Er^{3+} increased with the shortening of the decay time. Therefore, the increased population density of Mn^{2+} caused the decreased radiative transition rate of Er^{3+} ($^4\text{S}_{3/2}$ and $^2\text{H}_{11/2}$) turning down to ground state, resulting in an enhancement of red emission due to energy transfer from Mn^{2+} ($^4\text{T}_1$) to Er^{3+} ($^4\text{F}_{9/2}$) (Figure 4a). Meanwhile, the increased lifetime of Er^{3+} at 650 nm also verified the role of Mn^{2+} in energy transfer trace according to the decay curves of various content of Mn^{2+} (0%, 10%, 20%, 30%) (Figure 4b) [34].

Introducing transition metal ions with a long lifetime into conventional UCNPs is particularly attractive. The lifetime of Mn^{2+} ions could be modulated by crystal-site engineering. Liu et al. tuned the luminescence properties of Mn^{2+} in core-multishell nanoparticles by doping Ca^{2+} or Mg^{2+} , changing the output color from green to yellow and prolonging its lifetime [49]. The spin-forbidden transition of Mn^{2+} occurs between $^4\text{T}_1 \rightarrow ^6\text{A}_1$, allowing a longer fluorescence lifetime than lanthanide emitters. Because of the larger energy mismatch between Yb^{3+} and Mn^{2+} , the Yb^{3+} - Mn^{2+} dimer is difficult to form. However, Zhang et al. reported the successful preparation of Yb^{3+} - Mn^{2+} dimers,

obtaining a substantial long lifetime of Eu^{3+} (91 ms), while the normal UC lifetime of Eu^{3+} is only about 7 ms. In addition, there is a dynamic population balance between the energy state $|^2\text{F}_{7/2}, ^4\text{T}_1(4\text{G})\rangle(\text{Yb}^{3+}\text{-Mn}^{2+}$ dimers) and $^5\text{D}_0$ (Eu^{3+}), causing the sustained energy transferring from $\text{Yb}^{3+}\text{-Mn}^{2+}$ dimers to Eu^{3+} [50].

The long-lived Mn^{2+} integrated with the short-lived lanthanide particle platform could establish a new energy transfer pathway, and then affect the whole decay process. In a $\text{NaGdF}_4: 30\%\text{Mn}@\text{NaGdF}_4: 49\%\text{Yb}, 1\%\text{Tm}@\text{NaYF}_4$ nanoparticle, Gd sublattice-mediated energy migration facilitates Mn^{2+} upconversion luminescence, leading to a decrease in the lifetime of Gd^{3+} at 311 nm ($^6\text{P}_{7/2} \rightarrow ^8\text{S}_{7/2}$) from 6.5 to 4 ms (Figure 4c) [51]. As a result, the lifetime of lanthanide ions may be affected when the external ions introduced and interfered with the energy transfer channels.

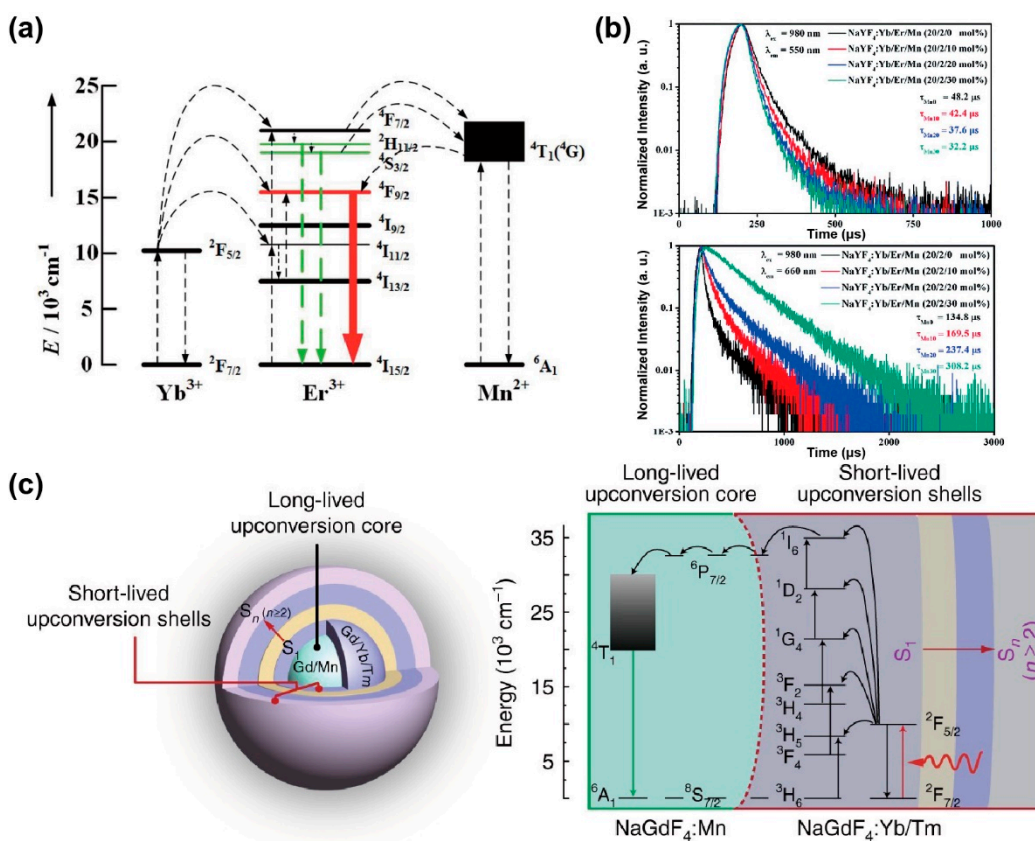


Figure 4. (a) The diagram for energy transfer mechanism among Yb^{3+} , Er^{3+} and Mn^{2+} under 980 nm excitation. (b) Luminescence decay curves of Er^{3+} at 550 nm and 650 nm in $\text{NaYF}_4: \text{Yb}^{3+}/\text{Er}^{3+}$ nanoparticles with different Mn^{2+} concentrations (0, 10, 20 and 30 mol%). Reproduced with permission from [34]. Copyright 2016, Royal Society of Chemistry. (c) Structural design of core–multishell nanoparticle and the energy transfer pathway among the Yb^{3+} , Tm^{3+} , Gd^{3+} and Mn^{2+} ions for the short- and long-lived upconversion luminescence under 980 nm excitation. Reproduced with permission from [51]. Copyright 2017, Nature Publishing Group.

Doping various amounts of Gd^{3+} into the NaYF_4 host nanocrystals could regulate the upconversion photoluminescence lifetimes. Xie et al. prolonged the lifetime of Er^{3+} ($^4\text{S}_{3/2} \rightarrow ^4\text{I}_{15/2}$, $^4\text{F}_{9/2} \rightarrow ^4\text{I}_{15/2}$) by utilizing the Gd^{3+} , substituting for Y^{3+} and Yb^{3+} in the crystal lattice of NaYF_4 host, which attributed to the energy transfer rate decrease caused by the average sensitizer-activator separation increasing [52].

2.4. Fluorescence Resonance Energy Transfer

An efficient energy transfer pathway could be established in fluorescence dye-loaded rare-earth nanocrystals, which enables luminescence lifetime tuning [53]. In contrast to

conventional molecular donor–acceptor pairs, the energy transfer efficiency is related to the distances between lanthanide-doped nanoparticles, and thus significantly depends on the nanoparticle diameter. Hirsch et al. synthesized NaYF₄: 20%Yb,2%Er with the precisely controlled size spanning from 10 to 43 nm, and coated with sulforhodamine B and rose bengal by ligand exchange. The nanoparticles with a mean diameter ranging from 20 to 25 nm possessed an optimum efficiency of 50–60%. The lifetime of Er³⁺ at 600 nm decreased primarily due to the competition of non-radiative surface deactivation at the smaller surface-to-volume ratios (Figure 5a) [54]. Li et al. loaded the IR-820 on NaYF₄: Tm to construct a FRET system. Luminescence decay from ³H₆→³H₄ transition was used as a detection signal. When the energy acceptor (IR-820) was attached to the donor (Tm³⁺: ³H₄) under 785 nm excitation, the lifetime of Tm³⁺ at 800 nm decreased because of luminescence resonance energy transfer (Figure 5b) [55]. Su et al. loaded the IR-806 on the NaGdF₄: 49%Yb,1%Tm@NaYF₄: 20%Yb@NaGdF₄: 50%Nd,10%Yb@NaGdF₄ nanoparticles to improve the ultraviolet luminescence intensity. With the back energy transferred from the nanoparticles to dye molecules, the decreased lifetimes of Gd³⁺ and Tm³⁺ ions were observed at 253, 276, 290, 310, 360 and 475 nm [56]. An organic fluorescent dye as an antenna could be used to broaden and increase absorption for UCNPs, allowing the energy to flow to dye molecules. Meanwhile, the hybrid system between dye molecules and UCNPs creates a new energy diffusion pathway, increasing the radiative transition process. Li et al. added the Cy3-SO₃ into a NaYF₄: 20%Yb,2%Er@CaF₂ solution to construct an energy dissipation channel, which could transfer energy to the dye by the radiative transition. As a result, the luminescence lifetime of Er³⁺ at 488 nm decreased with the concentration of Cy3-SO₃ increase (0.67, 2, 4, and 5.33 μM). The reduced lifetime value verified the non-radiative energy transfer process between Er³⁺ and Cy3-SO₃ [57].

The triplet excitons could be trapped by inter- or intra-molecular interactions and prolong organic phosphorescence. For example, Yb³⁺ luminescence could be generated by organic Yb³⁺ complexes and hybrid organic-conjugated Yb³⁺-doped nanoparticles. Ye et al. prepared a composite thin film, in which the Yb³⁺ ions are incorporated with tetrakis-(pentafluorophenyl)imidodiphosphinate to form the Yb(F-TPIP)₃ chelate, while zinc salt of 2-(tetrafluoro-2-hydroxyphenyl)tetrafluorobenzothiazole (Zn(F-BTZ)₂) served as the organic chromophore. The Zn(F-BTZ)₂ possessed the emission ranging from 450 nm to 900 nm under 405 nm excitation, and gave rise of the Yb³⁺ emission centered at 975 nm from the transition of Yb³⁺: ²F_{5/2}→²F_{7/2}. Note that the intrinsic lifetime of Yb³⁺ at 1 μm is about ~1 ms. The lifetime of sensitized organic Yb³⁺ compounds could prolong up to ~0.3 s. The prolonged emission lifetime was demonstrated by dynamic equilibrium due to the energy transfer process from long-lived organic triplet excitons [58].

The surface ligand coordination could reconstruct the crystal-field splitting and orbital hybridization, and narrow the gap of the 4d orbitals between inner and surface lanthanide sensitizers. For example, after the bidentate picolinic acid (2PA) molecules coordinated to NaGdF₄: Yb nanoparticles, a longer lifetime (289 μs) at 980 nm was observed. The results confirmed that 2PA molecules could activate the dark surface layers and facilitate energy migration in the Yb³⁺ sublattices. The Yb³⁺-2PA coupling facilitated energy migration by 4f-orbital energy resonance within the ytterbium sublattice, which can reduce surface defects to hinder energy diffusion. Density functional theory (DFT) verified that 2PA coating could narrow the gap between the superficial and inner Yb³⁺ by lowering the empty 4f levels. Rigid ligands also stabilized the excited state of superficial Yb³⁺, prevented the superficial lanthanide ions from the solvent and fluoride vacancy-induced quenching, and thus significantly suppressing multiphonon non-radiative decay (Figure 5c) [59].

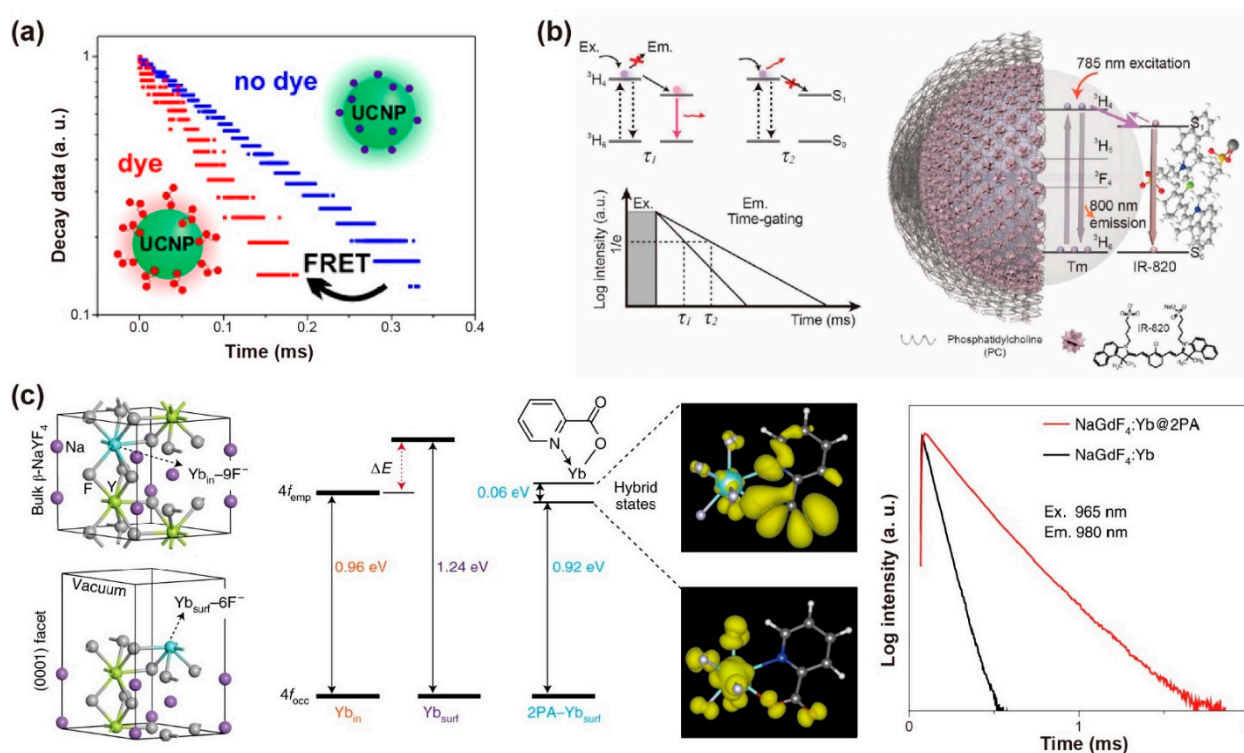


Figure 5. (a) Schematic diagram of the lifetime changing due to the existence of FRET process from UC-NPs to dye molecules. Reproduced with permission from [54]. Copyright 2017, American Chemical Society. (b) Schematic representation of the structure of the NaYF₄: Tm@PC-IR-820 nanocomposites, the absorbance and emission in the same transition (3H_6 – 3H_4) of NaYF₄: Tm nanoparticles and the variation of lifetime affected by the amount of IR-820 dye molecules. Reproduced with permission from [55]. Copyright 2019, WILEY-VCH. (c) The optimized structure shows ytterbium atoms located in the interior (Yb_{in}) and exterior (Yb_{surf}) position, the simulated 4f energy levels of ytterbium atoms, the spatial distribution of the charge densities for coupling states and the lifetime decay curves of Yb³⁺ at 980 nm with and without 2PA capping on the NaGdF₄: 5%Yb nanoparticles (10 nm) excited at 965 nm. Reproduced with permission from [59]. Copyright 2021, Nature Publishing Group.

2.5. Changing Temperature

The synthesized process would affect the crystallinity, phase state and volume of nanoparticles and thus influence the decay behaviors. Vatsa et al. studied the decay process of GdVO₄: Dy³⁺ nanoparticles after heat treatment. When heated from 500 °C to 900 °C, the lifetime of Dy³⁺ ($^4F_{9/2}$ level) extended from 114 μ s to 260 μ s due to the reduction of the non-radiative process by surface inhomogeneities. This increase in lifetime can also be ascribed to the decrease in the surface defects with the particle size increases in the heat treatment process (Figure 6a) [60]. For YVO₄: Ln³⁺ (Ln³⁺ = Dy³⁺, Eu³⁺) nanoparticles, the increase in covalent bond interaction caused by heat treatment led to a red shift in V–O charge transfer (CT). Similarly, the lifetimes of Dy³⁺ at $^4F_{9/2}$ and Eu³⁺ at 5D_0 increase with temperature from 500 °C to 900 °C due to the reduction of the non-radiative process on the surface of the particles [61].

As is well known, the decay time constant is inversely proportional to the radiative and non-radiative transition rates in the cross-relaxation process. The luminescence lifetime decreases with the increase of ambient temperature in most cases. The decay time with specific emissions produced by radiative transition rarely varies with temperature, while the non-radiative decay rate changes significantly with temperature [62]. For example, the lifetime of Yb³⁺ at 1000 nm reduced from $470 \pm 11 \mu$ s to $390 \pm 12 \mu$ s in NaYF₄: Nd³⁺, Yb³⁺ nanoparticles as the temperature rose from 25 °C to 45 °C. While the thermal coefficient α_τ calculated by the TGI system was almost unchanged ($-0.0092 \sim -0.010 \text{ } ^\circ\text{C}^{-1}$)

(Figure 6b,e) [63]. Moreover, cross-relaxation between Tm^{3+} ($^1\text{G}_4$) usually occurs when raising the emitter concentration or temperature. Yu et al. compared the sensitivity of $\beta\text{-PbF}_2\text{:Tm}^{3+}/\text{Yb}^{3+}$ with different Tm^{3+} doping concentrations. They found that the relative sensitivity maximum values of $^1\text{G}_4$ state lifetime in 0.0005Tm, 0.01Tm and 0.05Tm nanoparticles are $0.16\%K^{-1}$, $0.26\%K^{-1}$ and $0.46\%K^{-1}$ at 488K, respectively, indicating the potential ability as an indicator of upconversion luminescence lifetime-based thermometer [64].

In addition, the host matrix has a significant effect on thermal sensitivity. Díaz et al. found that oxide materials are more sensitive than fluoride ones by comparing the decay curves of $\text{NaYF}_4\text{:Er,Yb}$ and $\text{NaY}_2\text{F}_5\text{:Er,Yb}$ nanoparticles at room temperature and 60°C . [65]. The temperature dependency of Yb^{3+} emission lifetime in $\text{NaYF}_4\text{:Yb}^{3+}$, $\text{Nd}^{3+}\text{:CaF}_2$ nanoparticles was determined by the energy transfer and back energy transfer rate, the energy migration process (among Yb^{3+}), as well as radiative and non-radiative transition. Both the concentration of Nd^{3+} and Yb^{3+} affected the temperature sensitivity by changing the distance of $\text{Yb}^{3+}\text{-Yb}^{3+}$ and $\text{Yb}^{3+}\text{-Nd}^{3+}$, which in turn affected the back energy transfer processes from Yb^{3+} to Nd^{3+} and energy migration between Yb^{3+} ions. $\text{NaYF}_4\text{:20\%Yb}^{3+},60\%\text{Nd}^{3+}\text{:CaF}_2$ as the nanoprobe possessed optimum thermal sensitivity through varying doping concentrations of Yb^{3+} and Nd^{3+} , in which the lifetime of Yb^{3+} at 980 nm descended from 898 μs to 450 μs when the temperature increased from 10°C to 64°C . (Figure 6c,f) [66].

Interestingly, Li et al. demonstrate the lifetime compensation with temperature in $\text{NaErF}_4\text{:NaGdF}_4$ core-shell nanoparticles. The temperature-independent lifetime is attributed to the balance between lattice expansion (prolonging the lifetime) and thermal quenching (shortening the lifetime). A considerable energy migration process occurs in the high-doping concentration of Er^{3+} , and the efficiency is proportional inversely to the average donor-acceptor distance with sixth order of magnitude. As a consequence, elevated temperature induces the lattice to expand, leading to a longer transfer distance, and ultimately prolonging the lifetime of Er^{3+} . However, the prolonged lifetime caused by lattice expansion compensated for the difference value of the shorter lifetime aroused by thermal quenching, resulting in the temperature-independent lifetime (Figure 6d) [67].

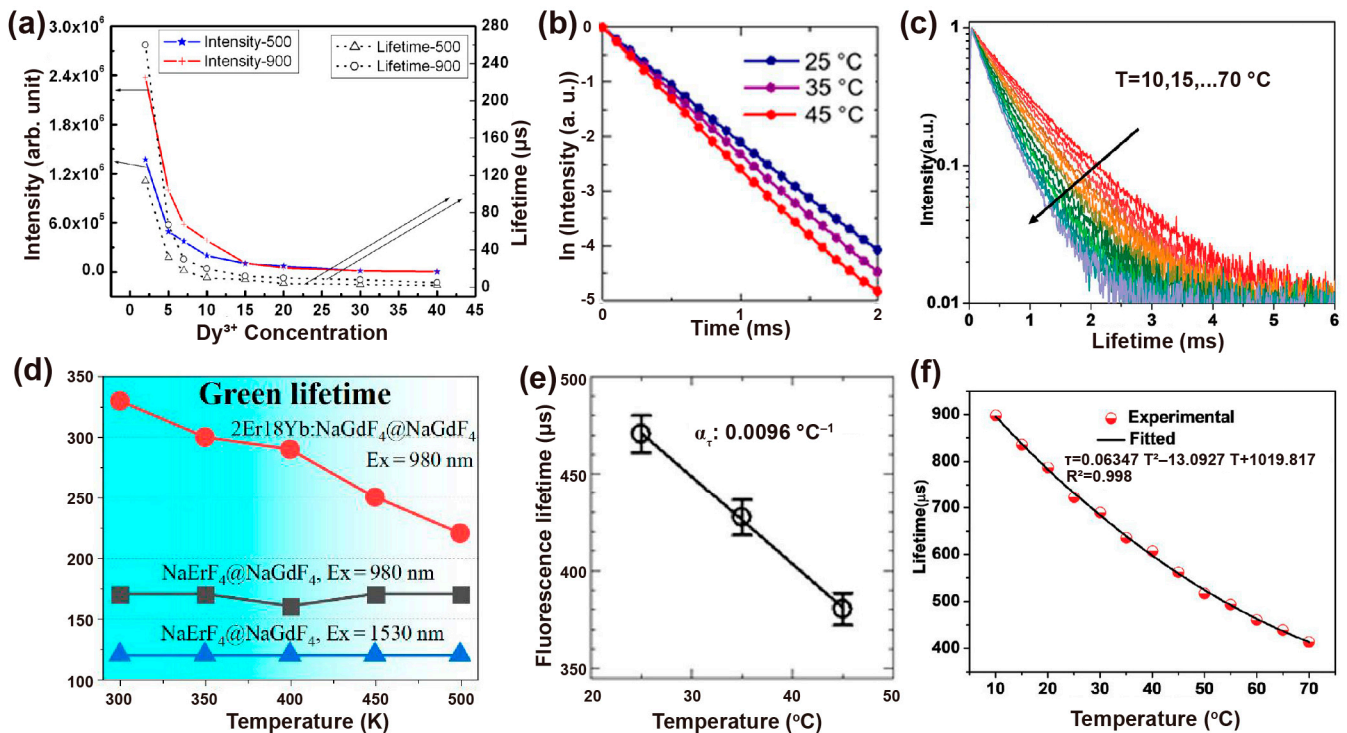


Figure 6. (a) Intensity (left) and the corresponding decay lifetime of Dy^{3+} at $^4\text{F}_{9/2}$ states (right) with the dependent variable of Dy^{3+} concentration when excited at 310 nm. Reproduced with permission

from [60]. Copyright 2009, AIP Publishing. (b) Luminescence decay curves of NaYF₄: Nd³⁺, Yb³⁺ at different experimental temperatures and (e) the corresponding calibration curve of temperature vs. luminescence lifetime. Reproduced with permission from [63]. Copyright 2019, Nature Publishing Group. (c) The decay curves of the measured NaYF₄@NaYF₄: 20%Yb³⁺, 60%Nd³⁺@CaF₂ nanoprobe at various temperatures and (f) corresponding nonlinear fitted curves between measured lifetime and temperature ranging from 10 °C to 70 °C. Reproduced with permission from [66]. Copyright 2020, WILEY-VCH. (d) Negative correlation curves of the lifetime of Er³⁺ at ⁴S_{3/2} versus ambient temperature for NaErF₄@NaGdF₄ and NaErF₄: 18%Yb, 2%Er@NaGdF₄ nanoparticles. Reproduced with permission from [67]. Copyright 2020, MDPI.

3. Bioapplications

With proper surface functionalization, lanthanide-doped nanoparticles possessed good biocompatibility and low toxicity [68]. Additionally, the pulsed laser illumination has a lower thermal effect than continuous-wave laser emission, which was harmful in biological applications [23]. Therefore, lanthanide-doped nanoprobe combined with lifetime sensing technology involving time-gated and lifetime coded imaging is widely used in biology and medicine [18]. This review gives a perspective of lifetime-based sensing and imaging in biological applications at molecule, cell, organ and living body levels.

3.1. Ions and Molecules Detection

The quantitative detection of targets based on intensity was unreliable due to the inhomogeneous scattering and absorption. Utilizing the lifetime variation of donor and acceptor, lifetime sensing based on the FRET mechanism could monitor ions' concentration accurately. Zhang et al. integrated the Nd³⁺-doped nanoparticle (energy donor) and MY-1057 (energy acceptor) to detect peroxynitrite (ONOO⁻) in the tumor-microenvironment based on the lifetime of NIR-II emission. The luminescence lifetime of the nanosensor at 1060 nm shortened with the increase in the amount of the surface dye molecules. The energy acceptor MY-1057 was destructed after reacting with reactive nitrogen species (especially ONOO⁻), resulting in the lifetime being recovered. Furthermore, the lifetime of the nanosensor would recover from 202 μs to 303 μs continuously after ONOO⁻ addition, showing linearity corresponding to ONOO⁻ concentration while independent of the penetration depth (0, 2, 5 mm). As a result, the ONOO⁻ concentration could be measured under unknown tissue penetration depth on a basis of standard curve due to the reliable lifetime-based ONOO⁻ detection (Figure 7a) [69]. Besides, Li et al. synthesized a lifetime-responsive nanocomposite consisting of NaYF₄: Tm nanoparticles and IR-820 dye molecules. The energy transfer from Tm³⁺-doped nanocrystal to IR-820 provided a tunable luminescence lifetime. ClO⁻ can destruct the dye and recover the lifetime of Tm³⁺. Based on lifetime changes, the concentration of ClO⁻ could be detected (Figure 7c) [55].

Time-resolved fluorescence microscopy could monitor target fluorescence by distinguishing the differences of fluorescence lifetimes in the nanosecond regime. For metal ions, Zhang et al. utilized the time-resolved fluorescence signals of BSA/Tb³⁺ to detect metal ions, involving Cu²⁺, Co²⁺, Zn²⁺, Mn²⁺, Ni²⁺, Pb²⁺, Ag⁺, Li⁺, Na⁺, Fe³⁺, Ca²⁺, Mg²⁺, Al³⁺, K⁺, Cd²⁺, Cr³⁺ and Hg²⁺ in two pH buffers (7.4 and 8.5). A 2000 μs gate time and a 50 μs delay time were settled for time-resolved fluorescence spectra by recording at 548 nm. Furthermore, the sensing platform could distinguish the various concentrations of the identical metal ions and the variety of metal ions mixture, even in biofluids [70]. Nagano et al. designed luminescent Eu³⁺ complexes (Eu-7) for time-resolved, long-lived luminescence microscopy (TRLLM). With Eu-7 injecting into a single Hela cell, the lifetime window centered at 617 ± 37 nm of Eu³⁺-based luminescence was collected under 360 ± 40 nm excitation. An increased luminescence enhancement was observed when the intracellular Zn²⁺ mixed with pyridithione, and decreased with the addition of cell-membrane-permeable chelator TPEN (N,N,N',N'-tetrakis(2-picolyl)ethylenediamine). As the delay times prior to counting and gate time were 70 and 808 μs, respectively, the intracellular Zn²⁺ con-

centration variation in living cells could be examined by using the TRLLM system with Zn^{2+} -sensitive luminescent lanthanide probe [Eu-7] (Figure 7b) [71].

Li et al. designed a water-soluble nanocomposite $NaYF_4: 5\%Nd$ and dye Cy860 enveloped by phosphatidylcholine (NPs@dye@PC). The Cy860 dye can quench the luminescence of lanthanide-doped nanoparticles. After hypochlorous acid (HClO) reacted with organic dye molecules, the quenching process was broken, and the luminescence of lanthanide-doped nanoparticles was recovered. Meanwhile, the lifetime of Nd^{3+} at 893 nm was shortened from 51 μs to 16 μs due to the FRET and inner filter effect. Utilizing the time-gated technique and signal collection method, they used $NaYF_4: Nd@Cy860@PC$ nanoprobe to detect the concentration of HClO in a living mouse model. Of note, the average relative deviations of HClO concentration were only 0.61% and 1.74% via ratio-metric detection, while the tissue depth increased up to 2mm and 3 mm, respectively (Figure 7d) [72]. Yuan et al. designed and synthesized a time-gated luminescence TGL probe (TR-HClO) for specific detection of HClO, in which luminescent Tb^{3+} (energy donor) nanoparticles were conjugated with a rhodamine derivative (energy acceptor). After reacting with HClO, the rhodamine emission at 580 nm increased while the Tb^{3+} emission at 540 nm decreased, resulting in an increase in the TGL intensity proportion of rhodamine to Tb^{3+} (I_{560}/I_{540}) up to ~ 9 -fold. The luminescence lifetime of Tb^{3+} decreased from 588 μs to 254 μs due to the FRET process and has excellent linearity of the variation of HClO concentration from 0.5 μM to 30 μM ($r = 0.99$). With dual signal outputting by ratio-metric TGL and luminescence lifetime, TR-HClO was applied to determine HClO in HepG2 cells [73].

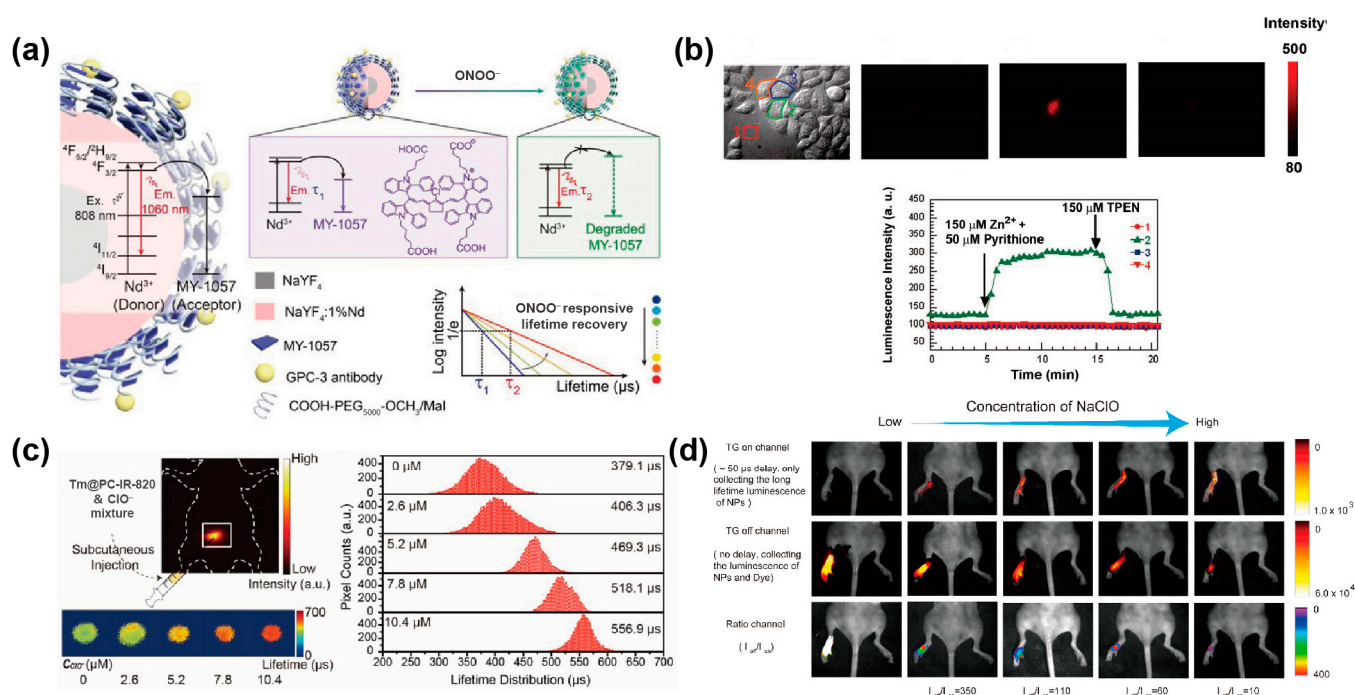


Figure 7. (a) Schematic diagram of nanosensor DSNP@MY-1057-GPC responding to ONOO⁻. Reproduced with permission from [69]. Copyright 2020, WILEY-VCH. (b) Time-resolved luminescence imaging of Zn^{2+} in living HeLa cells. Reproduced with permission from [71]. Copyright 2007, American Chemical Society. (c) Simulated luminescence lifetime imaging of the detection of responsive ClO^- . Reproduced with permission from [55]. Copyright 2019, WILEY-VCH. (d) The images of living mice in vivo with injection of 25 μL sodium hypochlorite solution and 25 μL $NaYF_4: Nd@Cy860@PC$ aqueous solution (3 mol/L). Reproduced with permission from [72]. Copyright 2019, American Chemical Society.

Vitamin C distribution and dynamic activities could be monitored by the time-gated luminescence microscopy. Yuan et al. developed a probe responding to ascorbic acid

(vitamin C) conjugating two nitroxide radicals and a luminescent europium complex. The nitroxide radicals prevented the probes from emitting luminescence until vitamin C was added to form a hydroxylamine derivative. The probes responded to vitamin C concentration linearly with a limit of detection (LOD) of 9.1 nM, which is lower than electrochemical methods by two orders of magnitude. The method of time-gated luminescence microscopy enabled real-time and specific monitoring of the cellular uptake, endogenous production and mapping of vitamin C in living *Daphnia magna* with free background [74].

3.2. DNA Detection

The pathogen DNA strands could be detected by using lifetime coding and decoding with downconversion lanthanide luminescence in microspheres. Jin et al. encapsulated a trivalent europium complex of thenoyltrifluoroacetate Eu (donor) and a hexafluorophosphate salt of cationic coumarin 50 (acceptor dyes) into porous polystyrene beads by solvent swelling. The average donor-to-acceptor distance could be manipulated by stepwise varying their concentrations, achieving the fine-tuned lifetimes of the microspheres. They carried out a biological experiment for high-throughput simultaneous detection of different pathogen DNAs (single strands), including human immunodeficiency virus, Ebola virus, hepatitis B virus and human papillomavirus (HPV) 16. The pathogen DNAs were added into the test panel composed of five types of conjugated microspheres encoded with different life spans, and Qdot 565 was added as a reporter dye. With the time-resolved orthogonal scanning automated microscopy analysis, the lifetime of Eu^{3+} complex in lanthanide-encoded microspheres were recovered by detecting the time-gated luminescence, which can identify their types of pathogen DNAs by decoding the lifetimes (Figure 8a) [75].

Similarly, Zhang et al. synthesized a series of nanoparticles with a settled lifetime by regulating the doped proportion of activators and the thickness of the energy migration layer. These nanoparticles were loaded into microspheres and modified by the DNA probe with nine high-risk HPV subtypes. With fluorescence dye 6-carboxyfluorescein as the reporter for DNA detection, the nanoparticles modified with DNA probe were added into a solution including PCR amplified DNAs of HPV targets. The HPV positive sample both of HPV 16 and HPV 18 could be distinguished by using the time-resolved imaging scanning system (Figure 8b) [42].

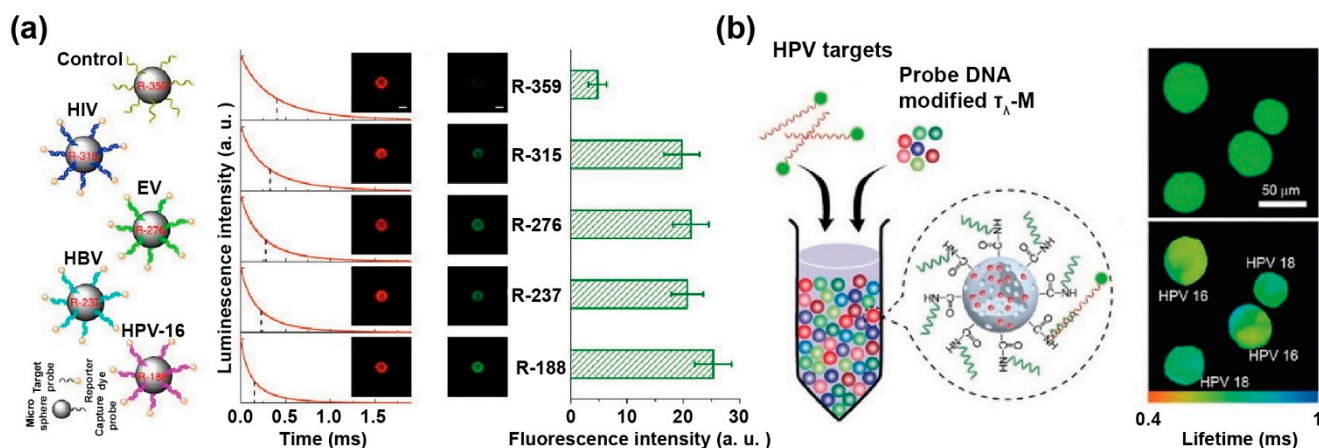


Figure 8. (a) Diagram of the five types of Eu-LRET microspheres conjugated to five different DNA sequences, in which the microspheres and amounts of pathogen DNAs were confirmed by the luminescence decay curves of Eu^{3+} and reporter fluorescence intensities, respectively. Reproduced with permission from [75]. Copyright 2014, Nature Publishing Group. (b) Schematic diagram of $\tau_{\lambda}\text{-M}$ for detecting HPV subtypes, and the confocal images with the corresponding lifetime images after incubating complementary target DNAs, respectively. Reproduced with permission from [42]. Copyright 2018, WILEY-VCH.

3.3. Protein Detection

A strategy to detect protease is to utilize lanthanide nanoprobe, which exhibit the long lifetimes and strong luminescence in the presence of an amino group, and a reverse trend with the protection of acyl groups. Kikuchi et al. synthesized lanthanide-based antenna-chelator conjugates with aniline derivative groups as the antennas. This conjugation has strong luminescence and a long lifetime (1.5 ms) at 350 nm when calpain I and leucine aminopeptidase (LAP) are added. These probes could exclude background fluorescence signals, suitable for detecting protease activities such as LAP and calpain I by time-resolved assays [76].

Similarly, Kikuchi et al. prepared a luminescent lanthanide probe TPA-Eu using time-resolved luminescence microscopy for protein imaging. The lifetime was 1.25 ms at 616 nm, which could be applied to detect TPA-Eu labeled on cell-surface proteins. The long lifetime could effectively separate the live-cell imaging from background signals (Figure 9a) [77]. Vuojola et al. constructed a hybrid FRET system consisting of Tb³⁺ with lanthanide-binding peptide (LBP) and green fluorescent protein (GFP). LBP can prolong the emission lifetime and can be applied in time-gated detection. After LBP and GFP were digested by enzyme, the long-lived sensitized acceptors were removed. The variation of the time-gated signals of terbium at 545 nm and the sensitized acceptor emission at 520 nm were monitored and used to detect the presence of caspase-3 inhibitor Z-DEVD-FMK [78].

The time-resolved detection could trace the biomolecules such as avidin with FRET biosensor, which can eliminate the background signals and improve the sensitivity. Chen et al. designed a hybrid system; NaYF₄: Ce/Tb nanocrystals could transfer the energy to fluorescein isothiocyanate (FITC). The lifetime of Tb³⁺ at ⁵D₄ decreased with the concentration of avidin improving from 0 to 500 nM. Using the model system, they could achieve an LOD of 5 nM (Figure 9b) [79]. By utilizing time-resolved fluorescence resonance energy transfer (TR-FRET), the avidin could be detected with the detection limit of 3.0 nM by using ZrO₂ NP bioprobes [80]. In addition, Chen et al. synthesized CaF₂: Ln³⁺ (Ln = Ce, Tb; Yb, Er; Yb, Tm) NPs with a size of sub-10 nm, which could sensitively detect avidin in homogeneous TR-FRET bioassays. Due to great spectral overlap, amino terminal fragment (ATF) coupled with CaF₂: Ce, Tb NP (emitting at 491 nm) labeled FITC (emitting at 490 nm) for TR-FRET detection. Therefore, the excitation energy of CaF₂: Ln³⁺ could be transferred to nearby FITC on account of the specific bond between avidin and biotin. The TR-FRET signal was enhanced gradually at the expense of the Tb³⁺ signal as the amount of avidin increased. The calibration curve for avidin concentrations from 0.1 nM to 430 nM exhibits that the signal of FITC/Tb in TR-FRET increases with the avidin concentration. The LOD is approximately 164 pM, which is the lowest detection limit for bioprobes on the basis of Ln³⁺-doped inorganic nanoparticles. Specially, they designed a system to detect soluble urokinase plasminogen activator receptor with ATF-coupled nanoparticles as the probes, whose LOD of tumor marker suPAR is 328 pM [81].

On the basis of the FRET mechanism, lanthanide nanoparticles can provide sensitive detection by using their decay time signals. Zhang et al. designed a hybrid system of UCNP-aptamer/ssDNA-pyropheophorbide-a (PPA)-doxorubicin (DOX) [UAS-PD] with 540 nm and 655 nm emission for targeted cancer therapy. The Black Hole Quencher-1 (BHQ-1) bore on ssDNA without the target cell. It could quench the luminescence of UCNPs at 540 nm due to FRET, but had a limited effect on 655 nm emission. A spontaneous conformational reorganization would occur when approaching specific cancer cells, moving ssDNA away from UCNPs and making PPA close to UCNPs. PPA decreased the luminescence intensity at 655 nm and recovered 540 nm emission due to FRET. Meanwhile, it affected the lifetime of both 540 nm and 655 nm. As a result, an extracellular cancer-specific biomarker PTK7 was developed to activate the UAS-PD as a probe. The lifetime of UAS-PD at 540 nm and 655 nm was measured to be 339.22 μs and 668.61 μs, respectively. Nevertheless, in the presence of PKT7, the lifetime of hybrid system increased by 476.33 μs at 540 nm, while the decay times at 655 nm decreased to 404.52 μs due to FRET from UAS-PD to BHQ-1 and

PPA. Specially, the ratiometric lifetime signal provided an extremely low LOD of 3.9 nM for PTK7 [82].

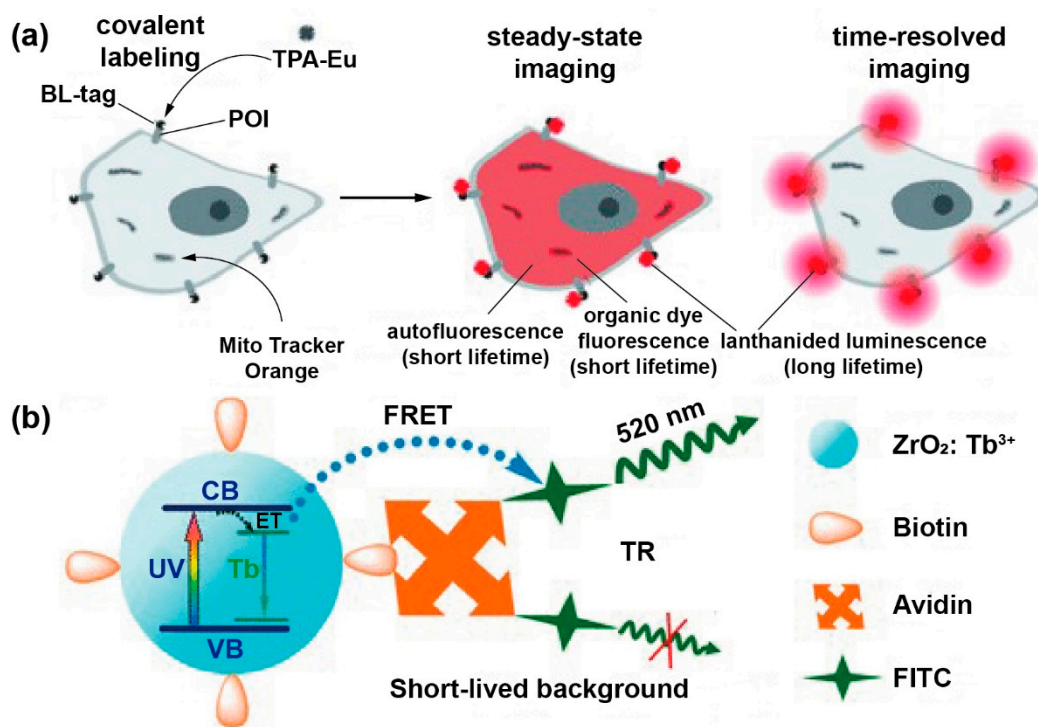


Figure 9. (a) Schematic representation of mutant β -lactamase-based protein labeling system, in which the luminescent lanthanide probe (TPA-Eu) was used for imaging cell-surface proteins (POIs). Reproduced with permission from [77]. Copyright 2011, WILEY-VCH. (b) Schematic diagram of TR-FRET detecting of avidin by employing biotinylated NCs (donor) and FITC (acceptor). Reproduced with permission from [79]. Copyright 2011, WILEY-VCH.

The sensitivity of immunoassays could be improved by using lanthanide-labeled nanoparticles with time-resolved immunofluorometric assays (TrIFA). Li et al. coated the luminescent Eu^{3+} and Tb^{3+} chelates covalently on the surface of silica nanoparticles to conjugate the antibodies or bind antibodies. As a comparison, the lifetime was no longer than 0.3 ms for Eu^{3+} -BHHCT after encapsulation in silica nanoparticles, while the lifetime of Tb^{3+} -BPTA chelates decreased prominently from 2.68 ms to 1.52 ms after encapsulation. The as-prepared conjugates in TrIFA could detect hepatitis B e antigen (HBeAg) and hepatitis B surface antigen (HBsAg). Utilizing the conjugates, the TrIFA for HBsAg possessed a comparable or lower LOD (0.0092 $\mu\text{g}/\text{L}$) than ELISA while the TrIFA for HBeAg possessed a much lower LOD (10.0 National Centre Unit (NCU)/L) than ELISA. By synchronizing TrIFA, the detection limits reached 0.033 $\mu\text{g}/\text{L}$ for HBsAg and 27.0 NCU/L for HBeAg, which is close to those of the individual assays [83].

3.4. Cell Labeling

Lanthanide bioprobes with time-gated detection enable rapid identification and quantification of cells bearing low-abundance surface biomarkers. $\text{CD}34^+$ cells are the hematopoietic stem cells, whose surface possesses the specific expression of CD34 protein. Jin et al. synthesized functionalized polystyrene nanoparticles containing europium and stained $\text{CD}34^+$ cells with a streptavidin–europium complex conjugate. Biotinylated anti-CD34 antibodies stained $\text{CD}34^+$ cells, and were imaged by time-gated luminescence, suppressing autofluorescence background signal (Figure 10a). As a result, the signal intensity was improved by a factor of ~ 20 , which could quantify the surface antigens of low expression on a single cell. Furthermore, with the assistance of an orthogonal scanning automated

microscopy, they obtained the quantitative statistical data of numerous CD4 cells on microscopy slides. They separated 98% target cell population from stained cells with a coefficient of variation of 31% [84].

Precise detection of tumor cells is critical for diagnosing early-stage cancer, forcing researchers to develop highly sensitive methods. The lifetime-resolved luminescent lanthanide technology could obtain high signal intensity by suppressing the background fluorescence. Chen et al. synthesized anti-EpCAM-antibody-modified NaEuF₄ NPs (NaEuF₄-Ab) to detect circulating tumor cells (CTCs) in whole blood samples without CTC enrichment. This amplified the signal through enhanced dissolution of time-resolved photoluminescence and elimination of short-lived autofluorescence interference. The detection of blood breast cells had a LOD of 1 cell/well in a 96-well plate. As a result, the direct detection of blood breast cancer cells has a detection rate of 93.9% (14/15 patients) in cancer patients. The time-resolved photoluminescence could improve the signal to noise ratio of the confocal laser scanning microscope (CLSM). It amplified the signal through the enhanced dissolution of time-resolved photoluminescence and elimination of short-lived autofluorescence interference. Comparing CLSM images of EpCAM-positive MCF-7 and EpCAM-negative HeLa cells incubated with NaEuF₄-Ab-TRITC for 1.5 h, the surface of MCF-7 cells emitted intense red luminescence but the surface of HeLa cells did not (Figure 10b) [85].

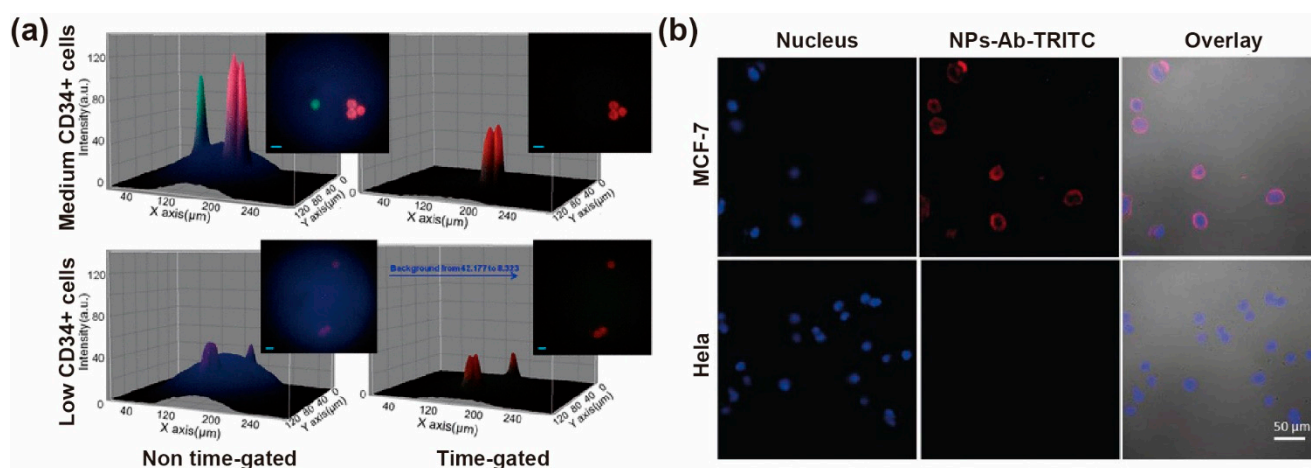


Figure 10. (a) The comparison of conventional UV fluorescence microscopy imaging (left) and time-gated luminescence microscopy imaging (right) of medium. Reproduced with permission from [84]. Copyright 2012, American Chemical Society. (b) Confocal laser scanning microscopy images of EpCAM-positive MCF-7 and EpCAM-negative HeLa cells incubated with NaEuF₄-Ab-TRITC for 1.5 h. Reproduced with permission from [85]. Copyright 2019, WILEY-VCH.

To increase the luminescent sensitivity, an effective strategy is to attach lanthanide chelates onto carrier molecules such as antibodies, which then were used to label surface antigens on cancer cells. Packer et al. developed a tetradentate β -diketonate-europium chelate for the immunodetection of prostate cancer cells (DU145). They conjugated MIL38 antibody to the chelate directly via lysine residues, and labeled a europium chelated secondary polyclonal antibody. As the DU145 cells (a prostate cancer cell line) were stained by conjugates, the time-gated luminescence microscopy was used to capture the images of immune-stained cancer cells while the cellular autofluorescence background was suppressed [86].

Another efficient method is to construct multiple lifetime channels, in which the lifetime could be precisely adjusted and detected. Zhang acquired a battery of Er-doped nanoparticles with settled lifetime at 1525 nm by control the thickness of energy relay layers and the concentration of activators. Three types of nanoparticles with settled lifetime were conjugated with primary antibodies to label the MCF-7 and BT-474 breast cancer cells, on a

basis of detecting the biomarkers of breast cancer including progesterone receptor (PR), oestrogen receptor (ER) and human epidermal growth factor receptor-2 (HER2). Due to the different expression patterns of the three biomarkers for the two tumor subtypes, the biomarker expressions of the tumor subtypes could be quantified by analyzing the three lifetime composites according to a pattern recognition algorithm. The highest expression in the MCF-7 tumors came from ER (62.3%), followed by PR (17.9%) and HER2 (19.8%). On the other hand, the BT-474 tumors expressed a large amount of HER2 (46.6%) but moderate levels of PR (28%) and ER (25.4%), which were in accordance with the standard ex vivo immunohistochemistry assays [43].

3.5. Organ Imaging

The practical use of UCNPs is still hampered by relatively shallow penetration depth. Comfortingly, lanthanide lifetime measurements are independent of tissue thickness, which can overcome the problem by lifetime coded technology. Chen et al. coated polyacrylic acid on a series of $\text{NaYF}_4@NaYbF_4@NaYF_4: Yb^{3+}/Tm^{3+}@NaYF_4$ via ligand exchange. They injected PAA-coated UCNPs (100 μL , 30 mg/mL) with the lifetime of 1158 μs into a Kunming mouse by tail vein injection, 20 μL of PAA-coated UCNPs (30 mg/mL) with lifetimes of 1528 μs and 920 μs into the right and left of the abdomen through subcutaneous injection, respectively. The time-delayed images were analyzed algorithmically by MATLAB. By taking advantage of temporal optical multiplexed upconversion with distinct lifetime-hued colors, liver and two abdomen subcutis could be seen clearly. The two close lifetimes could also be differentiated in in vivo imaging, indicating high temporal resolution abilities of the imaging system (Figure 11a,b) [41].

NIR-II luminescence has the advantage of reducing optical scattering. Er^{3+} emission at 1532 nm combined with lifetime sensing technology attracted specific attention. The fluorescent nanoprobes with Er^{3+} dopant in double interfaces ($\text{NaYF}_4@NaErF_4: Ce@NaYbF_4@NaErF_4: Ce@NaYF_4$) was designed by Zhang et al. to generate strong luminescence intensity and regulate the lifetime distinguishably. The nanoparticles decorated with phospholipid were administrated via oral, intertumoral and intravenous injection into mouse bearing with a subcutaneous tumor. Compared with other nanoparticles having larger luminescence intensity differences, these nanoprobes offered more accurate lifetime decoding for metabolically enriched organ imaging. During the 6 h monitoring period, it exhibited consistent characteristic lifetime compared with the agents in gut and tumor (Figure 11c) [87].

3.6. Thermal Sensing

Utilizing the temperature-dependent lifetime of lanthanide nanomaterials, lifetime-based thermometers have been developed to detect the temperature in the biologic microenvironment. Férid et al. synthesized $\text{La}_2\text{O}_3: Tm, Er, Yb$ UCNPs and used it as luminescent thermal probes to detect the temperature in the simulative biological tissue. The employed fluorescence lifetime is from the $^1G_4 \rightarrow ^3H_6$ transition of Tm^{3+} at 480 nm. UCNPs were placed at the same point on a biological tissue (0.15 mm thickness), and then were focalized by a 1450 nm heating diode laser and excited by a 980 nm pulsed laser. The fluorescence lifetime at 480 nm was measured with heating laser power varying from 30 mW to 130 mW. Hence, the sub-tissue temperature could be calculated by the achieved decay curves [88]. In an ex vivo experiment, a probe of water-dispersed $\text{NaY}_2\text{F}_5\text{O}: Er, Yb$ nanoparticles was injected into a chicken breast at 1 mm depth and heated by a laser beam. The luminescence decay curves excited by a 980 nm diode laser were recorded by a double beam confocal microscope. According to the calibration curves, the sub-tissue temperature could be determined by the level of a shortened lifetime [65].

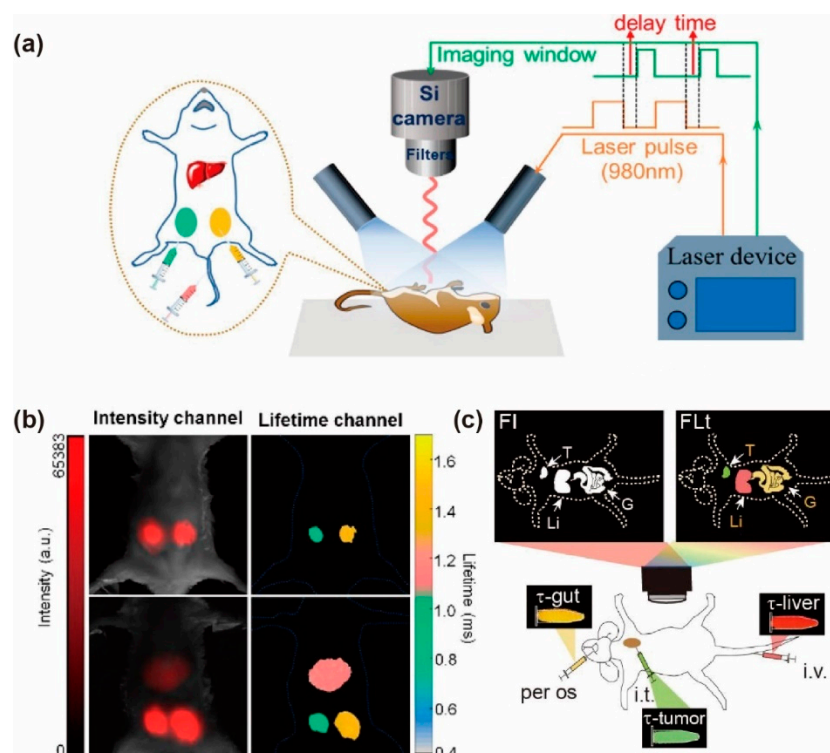


Figure 11. (a) Schematic diagram of nanoparticles with determined lifetime injecting into mouse, and then recorded by the home-built time-resolved luminescence imaging system. (b) The luminescence intensity (left) and lifetime (right) imaging of PAA-coated nanoparticles with two distinctive lifetimes injecting into a Kunming mouse and also into a second Kunming mouse (bottom). Reproduced with permission from [41]. Copyright 2020, American Chemical Society. (c) Schematic illustration of non-invasive NIR-II luminescence intensity and lifetime-based imaging for three diverse administration monitoring. Reproduced with permission from [87]. Copyright 2021, WILEY-VCH.

Integrating with QDs, the lanthanide upconversion nanomaterials exhibited excellent temperature sensing capability by utilizing arithmetic methods. Li et al. fabricated the hybrid upconversion nanoclusters (UCL-NCs) containing PbS QDs and NaYbF₄: 0.5%Tm@NaYF₄: 10%Yb@NaYF₄: 50%Nd (Tm-UCNPs) through an evaporation-induced self-assembly method. Both PbS QDs and Tm-UCNPs emitted around 810 nm through the upconversion process under 865 nm excitation. The lifetime of PbS QDs is responsive to the temperature at ns level, while the lifetime of Tm-UCNPs is fairly long, reaching a magnitude of μ s, and is independent of temperature. Pork tissue with different thicknesses mimics biological tissues to study the temperature variation of UCL-NCs. I_{sum} was obtained by the real-time imaging, and the I_{Tm} was acquired by a 20 μ s delayed time-resolved spectrometer. The experimental data was linearly fitted according to the ratio obtained from different thicknesses according to the formula $\text{Ratio} = (I_{\text{sum}} - I_{\text{Tm}})/I_{\text{Tm}}$. Furthermore, the UCL-NCs probe could apply in vivo to monitor intratumoral temperature, and the thermal sensitivity of the hybrid system reached 5.6%/K (Figure 12a) [89].

Dynamic temperature mapping in real-time is a powerful technology for wide-field photoluminescence lifetime imaging. Liang et al. designed a single-shot photoluminescence lifetime imaging thermometry (SPLIT), utilizing NaGdF₄: Er³⁺, Yb³⁺@NaGdF₄ nanoparticles as indicators. The lifetime of Er³⁺ red emission was more sensitive to temperature than the green emission, resulting from the larger energy separation between emitting and the lower-lying exciting states. Applied in longitudinal temperature monitoring successfully by overlaying chicken breast tissue, the SPLIT proved to be independent with tissue thickness and excitation light power density. When applied in a single-layer onion epidermis sample for single-cell temperature mapping, the lifetime/temperature maps were recorded in 3 s

measurement window (Figure 12b). The SPLIT was demonstrated to be resilient to spatial intensity variation, while being advantageous in handling temporal intensity variation [90].

The luminescence lifetime imaging in the NIR could be used for temperature sensing. In the experiment of Soga, the temperature was found to be independent with meat depth from 0 mm to 1.4 mm and luminescence intensity [63]. Li et al. designed a Nd-Yb co-doped nanothermometer to detect the temperature *in vivo*. The Nd³⁺ ions possess thermally rich energy levels to assemble responsive energy for the endogenous relative thermal response. In this structure, Yb³⁺ as energy acceptor was packed closely with Nd³⁺ in a nanocrystal with a diameter of 11 nm, owning tunable intensity and lifetime. The various lifetimes of Yb³⁺ (975 nm) corresponding to different temperatures could be observed due to energy transfer from ⁴F_{5/2} states of Nd³⁺ to Yb³⁺ under 793 nm excitation. The long circulation PEG modified nanoparticle was injected into a living mouse. After its footpad was stuck on a heat/cool pad through 793 nm excitation, the temperature difference could be distinguished between artery and vein, resulting from thermal relaxation. After stopping the heating process, the value of temperature loss was 10% in artery, and 25% in vein after 20 min. The lifetime of the optimized probe exhibited an excellent temperature sensitivity of 0.27 K *in vivo* [91].

Another nanothermometer was designed for sensing temperature utilizing the NIR-II luminescence lifetime of Yb³⁺ at 1000 nm, which is sensitive to temperature at different tissue depths. The NaYF₄@NaYF₄: Yb³⁺,Nd³⁺@CaF₂ with a size of 13.5 nm acted as a probe for detecting temperature *in vivo*. Due to back energy transfer from Yb³⁺ to Nd³⁺ and energy migration among Yb³⁺ ions, the doping concentration of Nd³⁺ and Yb³⁺ could affect the temperature sensitivity. NIR-II lifetime-encoded images are acquired by a NIR-sensitive InGaAs camera due to the precisely defined delay time set by the square-wave pulsed excitation laser. The luminescence lifetime versus temperature was calibrated by measuring a series of lifetime-hued images of nanoprobe solution. When the nanoprobe were injected into the inflamed and normal mouse, it exhibited a temperature difference of 2.3 °C according to a thermal camera. In addition, it showed a high-temperature sensitivity of 1.4–1.1% °C⁻¹ with the biological tissue up to 4 mm, ranging from 10 °C to 64 °C. The nanothermometers could diagnose murine inflammation *in vivo* based on lifetime responsiveness to temperature, and map the temperature distribution in the nanoparticle-probed area (Figure 12c) [66].

3.7. pH Sensing

It is well known that the pH-responsive fluorescein attached to UCNPs could detect pH by the ratiometric responses of emission intensity. Recently, a similar composite probe has been developed, which utilized the distinguished lifetime with the same emission wavelength to monitor a dynamic biological process [92]. Li et al. designed a NaYF₄: 1%Tm@NaLuF₄ and Rh760 (pH-responsive dye) composite to detect pH. UCNPs and dye molecules could emit luminescence at 800 nm under the 690 nm excitation, and the lifetimes were 695 μs and 1.40 ns, respectively. Moreover, the pH variation has a negligible effect on the lifetime in NaYF₄: 1%Tm@NaLuF₄ nanoparticles, but has a significant impact on the lifetime of Rh760. The time-gated technology could collect the long lifetime (UCNPs at 800 nm), while the short lifetime (Rh760 at 800 nm, only the level of ns) was blocked. Utilizing the time-gated sensing method, they developed a ratio signal of $F_{\text{steady-state}}/F_{\text{time-gated}}$ to detect pH. For example, they could sensitively monitor the pH value variation from 1.51 to 7.00 in 96-well plates covered with pork tissue, and proved the ratiometric lifetime was reversible and independent of nanoprobe concentration and excitation power density. Similarly, they successfully monitored the gastrointestinal pH value changes *in vivo* experiments (Figure 13a) [93].

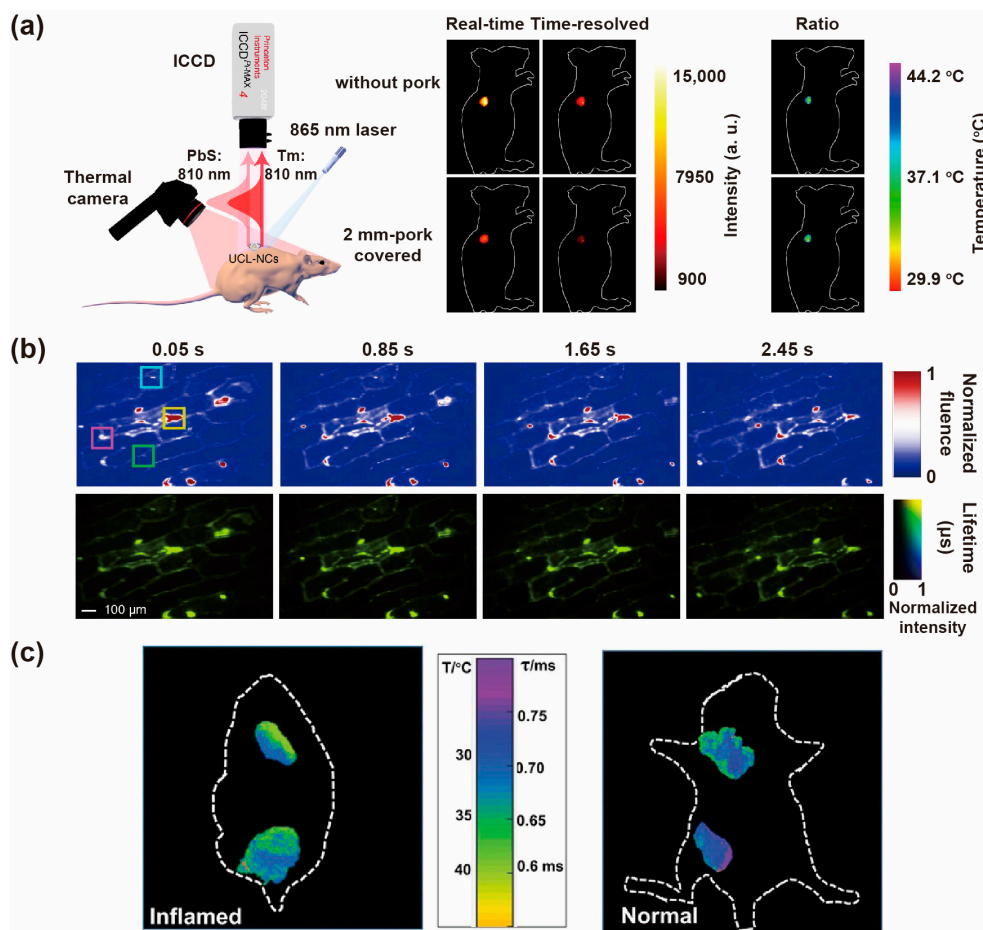


Figure 12. (a) Diagram of surficial and intratumoral detection in vivo and corresponding real-time, time-resolved and ratio UCL imaging without and with a 2 mm-pork slice covering under 865 nm excitation. Reproduced with permission from [89]. Copyright 2020, Nature Publishing Group. (b) The time-integrated images of a dynamic onion epidermis cell sample with labeling UCNP. Reproduced with permission from [90]. Copyright 2021, Nature Publishing Group. (c) Thermographic lifetime imaging of the nanosensors in the inflamed and normal mouse, showing the precise position of temperature distribution. Reproduced with permission from [66]. Copyright 2020, WILEY-VCH.

Designing an NIR lifetime (τ) probe (900–1700 nm) with different pH-responsive lifetimes is a synthetic challenge. Recently, Zhang et al. designed Yb³⁺ porphyrinate (F-Yb) as a pH-sensitive molecular probe. NIR emission and lifetime of Yb³⁺ increased with pKa values of ca. 6.6 from pH 9.0 and 5.0. The lifetime at 1000 nm was prolonged from 135 μ s to 170 μ s with pH from 5.0 to 1.0 due to reduced exposure to water and aggregation. Oral gavage experiments in nude mice were performed through the NIR τ probe F-Yb for in vivo pH detection. The lifetime of F-Yb in the stomach is 170 μ s and that in the intestine is 110 μ s. The pH values were 1.5 and 6.0 in the stomach and intestine, respectively. As a result, different organs could be distinguished with quantitative readouts by using the NIR τ probe F-Yb in time-resolved fluorescence lifetime imaging (Figure 13b) [94].

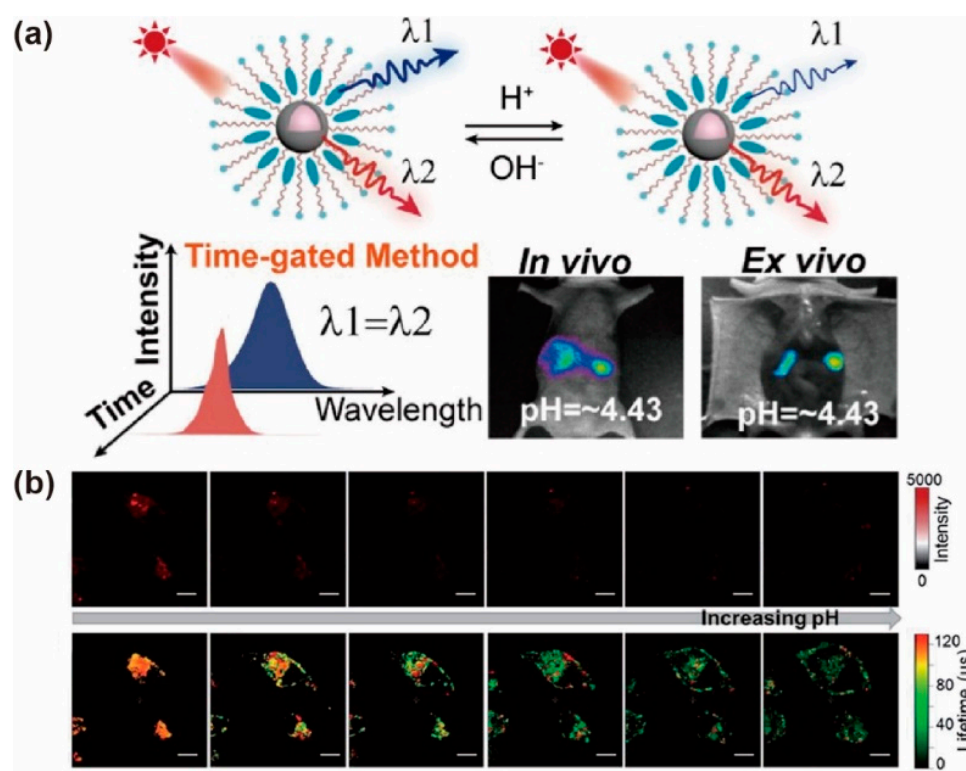


Figure 13. (a) The schematic representation and mechanism of the composite probe reversibly responds to variation in the microenvironment and emits two luminescence emissions with different lifetimes. The images of the gastrointestinal area with different pH values in vivo or ex vivo. Reproduced with permission from [93]. Copyright 2020, American Chemical Society. (b) The confocal luminescence images (top) and time-resolved luminescence lifetime images (bottom) of F-Yb (10 μM , 4 h) in HeLa cells reacted with 0.5 μM chloroquine. Reproduced with permission from [94]. Copyright 2019, Royal Society of Chemistry.

4. Conclusions and Outlooks

Compared with traditional fluorescence detection, lifetime sensing based on the lanthanide nanomaterials is not susceptible to tissue thickness, laser power intensity, background interference and solution concentration. Furthermore, the signal can be enhanced by methods such as time-gated lifetime imaging, ratiometric detection and lifetime-coded technology. While the strategies based on measuring the lifetime signal changes in lanthanide-doped nanomaterial for biodetection and bioimaging have promising prospects, there exist many technical challenges to be overcome in practical application. For example, the nanoprobe's luminescence intensity should be further increased to improve the lifetime signal acquisition speed. It can be solved by optimizing the concentration of dopant, core-shell structure and antenna addition. Moreover, it is highly desirable to increase the stability in the biological microenvironment. Numerous composite nanoprobe consist of lanthanide nanoparticles and molecules such as dye, fluorescein, etc., which are susceptible to their surroundings. Hence, it is necessary to develop stable nanoprobe and measurement techniques. Last but not least, the use of lifetime-based sensing technology could be extended to develop multimodality nanoplateforms with synergistic effects for diagnosis and treatment [95]. This technology will draw wider attention to the development trajectory of fundamental research and clinical applications in luminescent materials.

Author Contributions: Conceptualization, Q.S.; validation, Q.S. and C.H.; investigation, M.W.; writing—original draft preparation, M.W.; writing—review and editing, Q.S. and C.H.; supervision, Q.S. and C.H. All authors have read and agreed to the published version of the manuscript.

Funding: This research was funded by the National Natural Science Foundation of China (Nos. 82002893 and 21701109) for financial supports.

Institutional Review Board Statement: Not applicable.

Informed Consent Statement: Not applicable.

Data Availability Statement: Data are contained within the article.

Conflicts of Interest: The authors declare no conflict of interest.

References

1. Seaberg, J.; Montazerian, H.; Hossen, M.N.; Bhattacharya, R.; Khademhosseini, A.; Mukherjee, P. Hybrid Nanosystems for Biomedical Applications. *ACS Nano* **2021**, *15*, 2099–2142. [[CrossRef](#)] [[PubMed](#)]
2. Liu, X.; Braun, G.B.; Qin, M.; Ruoslahti, E.; Sugahara, K.N. In Vivo Cation Exchange in Quantum Dots for Tumor-specific Imaging. *Nat. Commun.* **2017**, *8*, 343. [[CrossRef](#)] [[PubMed](#)]
3. Liu, Q.; Zhang, Y.; Peng, C.S.; Yang, T.; Joubert, L.-M.; Chu, S. Single Upconversion Nanoparticle Imaging at Sub-10 W cm⁻² Irradiance. *Nat. Photon.* **2018**, *12*, 548–553. [[CrossRef](#)] [[PubMed](#)]
4. Chen, S.; Xiong, C.; Liu, H.; Wan, Q.; Hou, J.; He, Q.; Badu-Tawiah, A.; Nie, Z. Mass Spectrometry Imaging Reveals the Sub-organ Distribution of Carbon Nanomaterials. *Nat. Nanotechnol.* **2015**, *10*, 176–182. [[CrossRef](#)] [[PubMed](#)]
5. Swallow, J.G.; Kim, J.J.; Maloney, J.M.; Chen, D.; Smith, J.F.; Bishop, S.R.; Tuller, H.L.; Van Vliet, K.J. Dynamic Chemical Expansion of Thin-film Non-stoichiometric Oxides at Extreme Temperatures. *Nat. Mater.* **2017**, *16*, 749–754. [[CrossRef](#)] [[PubMed](#)]
6. Adhikari, G.C.; Vargas, P.A.; Zhu, H.; Grigoriev, A.; Zhu, P. Tetradic Phosphor White Light with Variable CCT and Superlative CRI through Organolead Halide Perovskite Nanocrystals. *Nanoscale Adv.* **2019**, *1*, 1791–1798. [[CrossRef](#)]
7. Liu, Y.; Wang, Y.; Song, S.; Zhang, H. Tumor Diagnosis and Therapy Mediated by Metal Phosphorus-Based Nanomaterials. *Adv. Mater.* **2021**, *33*, 2103936. [[CrossRef](#)]
8. Zhang, K.; Gao, Y.-J.; Yang, P.-P.; Qi, G.-B.; Zhang, J.-P.; Wang, L.; Wang, H. Self-Assembled Fluorescent Organic Nanomaterials for Biomedical Imaging. *Adv. Healthc. Mater.* **2018**, *7*, 1800344. [[CrossRef](#)]
9. Zhu, X.; Li, J.; Qiu, X.; Liu, Y.; Feng, W.; Li, F. Upconversion Nanocomposite for Programming Combination Cancer Therapy by Precise Control of Microscopic Temperature. *Nat. Commun.* **2018**, *9*, 2176. [[CrossRef](#)]
10. Qiu, X.; Zhu, X.; Su, X.; Xu, M.; Yuan, W.; Liu, Q.; Xue, M.; Liu, Y.; Feng, W.; Li, F. Near-Infrared Upconversion Luminescence and Bioimaging In Vivo Based on Quantum Dots. *Adv. Sci.* **2019**, *6*, 1801834. [[CrossRef](#)]
11. Zhu, X.; Su, Q.; Feng, W.; Li, F. Anti-Stokes Shift Luminescent Materials for Bio-applications. *Chem. Soc. Rev.* **2017**, *46*, 1025–1039. [[CrossRef](#)] [[PubMed](#)]
12. Li, Y.; Sun, Y.; Li, J.; Su, Q.; Yuan, W.; Dai, Y.; Han, C.; Wang, Q.; Feng, W.; Li, F. Ultrasensitive Near-Infrared Fluorescence-Enhanced Probe for In Vivo Nitroreductase Imaging. *J. Am. Chem. Soc.* **2015**, *137*, 6407–6416. [[CrossRef](#)]
13. Bünzli, J.-C.G. Lanthanide Luminescence for Biomedical Analyses and Imaging. *Chem. Rev.* **2010**, *110*, 2729–2755. [[CrossRef](#)] [[PubMed](#)]
14. Richardson, D.S.; Lichtman, J.W. Clarifying Tissue Clearing. *Cell* **2015**, *162*, 246–257. [[CrossRef](#)] [[PubMed](#)]
15. Zebibula, A.; Alifu, N.; Xia, L.; Sun, C.; Yu, X.; Xue, D.; Liu, L.; Li, G.; Qian, J. Ultrastable and Biocompatible NIR-II Quantum Dots for Functional Bioimaging. *Adv. Funct. Mater.* **2018**, *28*, 1703451. [[CrossRef](#)]
16. Thor, W.; Wu, Y.; Wang, L.; Zhang, Y.; Tanner, P.A.; Wong, K.-L. Charging and Ultralong Phosphorescence of Lanthanide Facilitated Organic Complex. *Nat. Commun.* **2021**, *12*, 6532. [[CrossRef](#)] [[PubMed](#)]
17. Suhling, K.; French, P.M.W.; Phillips, D. Time-resolved Fluorescence Microscopy. *Photoch. Photobiol. Sci.* **2005**, *4*, 13–22. [[CrossRef](#)] [[PubMed](#)]
18. Zhang, K.Y.; Yu, Q.; Wei, H.; Liu, S.; Zhao, Q.; Huang, W. Long-Lived Emissive Probes for Time-Resolved Photoluminescence Bioimaging and Biosensing. *Chem. Rev.* **2018**, *118*, 1770–1839. [[CrossRef](#)]
19. Xie, Y.; Arno, M.C.; Husband, J.T.; Torrent-Sucarrat, M.; O'Reilly, R.K. Manipulating the Fluorescence Lifetime at the Sub-cellular Scale via Photo-switchable Barcoding. *Nat. Commun.* **2020**, *11*, 2460. [[CrossRef](#)]
20. Lu, Y.; Zhao, J.; Zhang, R.; Liu, Y.; Liu, D.; Goldys, E.M.; Yang, X.; Xi, P.; Sunna, A.; Lu, J.; et al. Tunable Lifetime Multiplexing Using Luminescent Nanocrystals. *Nat. Photon.* **2014**, *8*, 32–36. [[CrossRef](#)]
21. Lei, X.; Li, R.; Tu, D.; Shang, X.; Liu, Y.; You, W.; Sun, C.; Zhang, F.; Chen, X. Intense Near-infrared-II Luminescence from NaCeF₄: Er/Yb Nanoprobes for in vitro Bioassay and In Vivo Bioimaging. *Chem. Sci.* **2018**, *9*, 4682–4688. [[CrossRef](#)] [[PubMed](#)]
22. Liu, Y.; Gu, Y.; Yuan, W.; Zhou, X.; Qiu, X.; Kong, M.; Wang, Q.; Feng, W.; Li, F. Quantitative Mapping of Liver Hypoxia in Living Mice Using Time-Resolved Wide-Field Phosphorescence Lifetime Imaging. *Adv. Sci.* **2020**, *7*, 1902929. [[CrossRef](#)] [[PubMed](#)]
23. Zheng, X.; Zhu, X.; Lu, Y.; Zhao, J.; Feng, W.; Jia, G.; Wang, F.; Li, F.; Jin, D. High-Contrast Visualization of Upconversion Luminescence in Mice Using Time-Gating Approach. *Anal. Chem.* **2016**, *88*, 3449–3454. [[CrossRef](#)]

24. Ma, Q.; Wang, J.; Li, Z.; Lv, X.; Liang, L.; Yuan, Q. Recent Progress in Time-Resolved Biosensing and Bioimaging Based on Lanthanide-Doped Nanoparticles. *Small* **2019**, *15*, 1804969. [[CrossRef](#)] [[PubMed](#)]
25. Zheng, W.; Tu, D.; Huang, P.; Zhou, S.; Chen, Z.; Chen, X. Time-resolved Luminescent Biosensing Based on Inorganic Lanthanide-doped Nanoprobes. *Chem. Commun.* **2015**, *51*, 4129–4143. [[CrossRef](#)] [[PubMed](#)]
26. Bergstrand, J.; Liu, Q.; Huang, B.; Peng, X.; Würth, C.; Resch-Genger, U.; Zhan, Q.; Widengren, J.; Ågren, H.; Liu, H. On the Decay Time of Upconversion Luminescence. *Nanoscale* **2019**, *11*, 4959–4969. [[CrossRef](#)] [[PubMed](#)]
27. Quinet, P.; Palmeri, P.; Biémont, E.; Li, Z.S.; Zhang, Z.G.; Svanberg, S. Radiative Lifetime Measurements and Transition Probability Calculations in Lanthanide Ions. *J. Alloys Compd.* **2002**, *344*, 255–259. [[CrossRef](#)]
28. Kong, J.; Shang, X.; Zheng, W.; Chen, X.; Tu, D.; Wang, M.; Song, J.; Qu, J. Revisiting the Luminescence Decay Kinetics of Energy Transfer Upconversion. *J. Phys. Chem. Lett.* **2020**, *11*, 3672–3680. [[CrossRef](#)]
29. Lauhon, L.J.; Gudiksen, M.S.; Wang, D.; Lieber, C.M. Epitaxial Core-shell and Core-multishell Nanowire Heterostructures. *Nature* **2002**, *420*, 57–61. [[CrossRef](#)]
30. Hudry, D.; Howard, I.A.; Popescu, R.; Gerthsen, D.; Richards, B.S. Structure-Property Relationships in Lanthanide-Doped Upconverting Nanocrystals: Recent Advances in Understanding Core-Shell Structures. *Adv. Mater.* **2019**, *31*, 1900623. [[CrossRef](#)]
31. Zhao, J.; Lu, Z.; Yin, Y.; McRae, C.; Piper, J.A.; Dawes, J.M.; Jin, D.; Goldys, E.M. Upconversion Luminescence with Tunable Lifetime in NaYF₄: Yb,Er Nanocrystals: Role of Nanocrystal Size. *Nanoscale* **2013**, *5*, 944–952. [[CrossRef](#)] [[PubMed](#)]
32. Wang, Y.; Deng, R.; Xie, X.; Huang, L.; Liu, X. Nonlinear Spectral and Lifetime Management in Upconversion Nanoparticles by Controlling Energy Distribution. *Nanoscale* **2016**, *8*, 6666–6673. [[CrossRef](#)]
33. Su, Q.; Han, S.; Xie, X.; Zhu, H.; Chen, H.; Chen, C.-K.; Liu, R.-S.; Chen, X.; Wang, F.; Liu, X. The Effect of Surface Coating on Energy Migration-Mediated Upconversion. *J. Am. Chem. Soc.* **2012**, *134*, 20849–20857. [[CrossRef](#)] [[PubMed](#)]
34. Huang, Z.; Gao, H.; Mao, Y. Understanding the Effect of Mn²⁺ on Yb³⁺/Er³⁺ Upconversion and Obtaining a Maximum Upconversion Fluorescence Enhancement in Inert-core/active-shell/inert-shell Structures. *RSC Adv.* **2016**, *6*, 83321–83327. [[CrossRef](#)]
35. Li, Z.; Liu, H.; Wang, R.; Ji, C.; Wei, Y.; Shi, M.; Wang, Y.; Du, Y.; Zhang, Y.; Yuan, Q.; et al. Bioactive Core-Shell CaF₂ Upconversion Nanostructure for Promotion and Visualization of Engineered Bone Reconstruction. *ACS Nano* **2020**, *14*, 16085–16095. [[CrossRef](#)] [[PubMed](#)]
36. Dong, H.; Sun, L.-D.; Li, L.-D.; Si, R.; Liu, R.; Yan, C.-H. Selective Cation Exchange Enabled Growth of Lanthanide Core/Shell Nanoparticles with Dissimilar Structure. *J. Am. Chem. Soc.* **2017**, *139*, 18492–18495. [[CrossRef](#)] [[PubMed](#)]
37. Tan, M.; del Rosal, B.; Zhang, Y.; Martín Rodríguez, E.; Hu, J.; Zhou, Z.; Fan, R.; Ortgies, D.H.; Fernández, N.; Chaves-Coira, I.; et al. Rare-earth-doped Fluoride Nanoparticles with Engineered Long Luminescence Lifetime for Time-gated In Vivo Optical Imaging in the Second Biological Window. *Nanoscale* **2018**, *10*, 17771–17780. [[CrossRef](#)]
38. Su, Q.; Wei, H.-L.; Liu, Y.; Chen, C.; Guan, M.; Wang, S.; Su, Y.; Wang, H.; Chen, Z.; Jin, D. Six-photon Upconverted Excitation Energy Lock-in for Ultraviolet-C Enhancement. *Nat. Commun.* **2021**, *12*, 4367. [[CrossRef](#)]
39. Huang, Q.; Ye, W.; Jiao, X.; Yu, L.; Liu, Y.; Liu, X. Efficient Upconversion Fluorescence in NaYF₄: Yb³⁺, Er³⁺/mNaYF₄ Multilayer core-shell Nanoparticles. *J. Alloys Compd.* **2018**, *763*, 216–222. [[CrossRef](#)]
40. Gu, Y.; Guo, Z.; Yuan, W.; Kong, M.; Liu, Y.; Liu, Y.; Gao, Y.; Feng, W.; Wang, F.; Zhou, J.; et al. High-sensitivity Imaging of Time-domain Near-infrared Light Transducer. *Nat. Photon.* **2019**, *13*, 525–531. [[CrossRef](#)]
41. Li, H.; Tan, M.; Wang, X.; Li, F.; Zhang, Y.; Zhao, L.; Yang, C.; Chen, G. Temporal Multiplexed In Vivo Upconversion Imaging. *J. Am. Chem. Soc.* **2020**, *142*, 2023–2030. [[CrossRef](#)] [[PubMed](#)]
42. Zhou, L.; Fan, Y.; Wang, R.; Li, X.; Fan, L.; Zhang, F. High-capacity Upconversion Wavelength and Lifetime Binary Encoding for Multiplexed Biodetection. *Angew. Chem.* **2018**, *130*, 13006–13011. [[CrossRef](#)]
43. Fan, Y.; Wang, P.; Lu, Y.; Wang, R.; Zhou, L.; Zheng, X.; Li, X.; Piper, J.A.; Zhang, F. Lifetime-engineered NIR-II Nanoparticles Unlock Multiplexed In Vivo Imaging. *Nature Nanotechnol.* **2018**, *13*, 941–946. [[CrossRef](#)] [[PubMed](#)]
44. Bartkowiak, A.; Runowski, M.; Shyichuk, A.; Majewska, M.; Grzyb, T. Tunable Yellow-green Up-conversion Emission and Luminescence Lifetimes in Yb³⁺-Er³⁺-Ho³⁺ Multi-doped β-NaLuF₄ Crystals. *J. Alloys Compd.* **2019**, *793*, 96–106. [[CrossRef](#)]
45. Siefe, C.; Mehlenbacher, R.D.; Peng, C.S.; Zhang, Y.; Fischer, S.; Lay, A.; McLellan, C.A.; Alivisatos, A.P.; Chu, S.; Dionne, J.A. Sub-20 nm Core-Shell-Shell Nanoparticles for Bright Upconversion and Enhanced Förster Resonant Energy Transfer. *J. Am. Chem. Soc.* **2019**, *141*, 16997–17005. [[CrossRef](#)]
46. Dong, H.; Sun, L.-D.; Wang, Y.-F.; Xiao, J.-W.; Tu, D.; Chen, X.; Yan, C.-H. Photon Upconversion in Yb³⁺-Tb³⁺ and Yb³⁺-Eu³⁺ Activated Core/shell Nanoparticles with Dual-band Excitation. *J. Mater. Chem. C* **2016**, *4*, 4186–4192. [[CrossRef](#)]
47. Liu, X.; Chen, Z.H.; Zhang, H.; Fan, Y.; Zhang, F. Independent Luminescent Lifetime and Intensity Tuning of Upconversion Nanoparticles by Gradient Doping for Multiplexed Encoding. *Angew. Chem.* **2021**, *133*, 7117–7121. [[CrossRef](#)]
48. Zhang, H.; Fan, Y.; Pei, P.; Sun, C.; Lu, L.; Zhang, F. Tm³⁺-Sensitized NIR-II Fluorescent Nanocrystals for In Vivo Information Storage and Decoding. *Angew. Chem. Int. Ed.* **2019**, *58*, 10153–10157. [[CrossRef](#)]
49. Liu, X.; Yi, Z.; Qin, X.; Liu, H.; Huang, W.; Liu, X. Tuning Long-Lived Mn(II) Upconversion Luminescence through Alkaline-Earth Metal Doping and Energy-Level Tailoring. *Adv. Opt. Mater.* **2019**, *7*, 1900519. [[CrossRef](#)]
50. Han, X.; Song, E.; Chen, W.; Zhou, Y.; Zhang, Q. Color-tunable Upconversion Luminescence and Prolonged Eu³⁺ Fluorescence Lifetime in Fluoride KCdF₃: Yb³⁺, Mn²⁺, Eu³⁺ via Controllable and Efficient Energy Transfer. *J. Mater. Chem. C* **2020**. [[CrossRef](#)]

51. Liu, X.; Wang, Y.; Li, X.; Yi, Z.; Deng, R.; Liang, L.; Xie, X.; Loong, D.T.B.; Song, S.; Fan, D.; et al. Binary Temporal Upconversion Codes of Mn²⁺-activated Nanoparticles for Multilevel Anti-counterfeiting. *Nat. Commun.* **2017**, *8*, 899. [[CrossRef](#)]
52. Qin, H.; Wu, D.; Sathian, J.; Xie, X.; Ryan, M.; Xie, F. Tuning the Upconversion Photoluminescence Lifetimes of NaYF₄: Yb³⁺, Er³⁺ through Lanthanide Gd³⁺ Doping. *Sci. Rep.* **2018**, *8*, 12683. [[CrossRef](#)] [[PubMed](#)]
53. Payne, N.C.; Kalyakina, A.S.; Singh, K.; Tye, M.A.; Mazitschek, R. Bright and Stable Luminescent Probes for Target Engagement Profiling in Live Cells. *Nat. Chem. Biol.* **2021**, *17*, 1168–1177. [[CrossRef](#)] [[PubMed](#)]
54. Muhr, V.; Würth, C.; Kraft, M.; Buchner, M.; Baeumner, A.J.; Resch-Genger, U.; Hirsch, T. Particle-Size-Dependent Förster Resonance Energy Transfer from Upconversion Nanoparticles to Organic Dyes. *Anal. Chem.* **2017**, *89*, 4868–4874. [[CrossRef](#)] [[PubMed](#)]
55. Kong, M.; Gu, Y.; Liu, Y.; Shi, Y.; Wu, N.; Feng, W.; Li, F. Luminescence Lifetime-Based In Vivo Detection with Responsive Rare Earth-Dye Nanocomposite. *Small* **2019**, *15*, 1904487. [[CrossRef](#)]
56. Wang, M.; Wei, H.; Wang, S.; Hu, C.; Su, Q. Dye Sensitization for Ultraviolet Upconversion Enhancement. *Nanomaterials* **2021**, *11*, 3114. [[CrossRef](#)]
57. Xue, M.; Cao, C.; Zhou, X.; Xu, M.; Feng, W.; Li, F. Tuning the Upconversion Efficiency and Spectrum of Upconversion Nanoparticles through Surface Decorating of an Organic Dye. *Inorg. Chem.* **2019**, *58*, 14490–14497. [[CrossRef](#)]
58. Lyu, C.; Li, H.; Wyatt, P.B.; Gillin, W.P.; Ye, H. Prolonged and Efficient Near-infrared Photoluminescence of a Sensitized Organic Ytterbium-containing Molecular Composite. *J. Mater. Chem. C* **2020**, *8*, 9502–9505. [[CrossRef](#)]
59. Xu, H.; Han, S.; Deng, R.; Su, Q.; Wei, Y.; Tang, Y.; Qin, X.; Liu, X. Anomalous Upconversion Amplification Induced by Surface Reconstruction in Lanthanide Sublattices. *Nat. Photon.* **2021**, *15*, 732–737. [[CrossRef](#)]
60. Singh, N.S.; Ningthoujam, R.S.; Yaiphaba, N.; Singh, S.D.; Vatsa, R.K. Lifetime and Quantum Yield Studies of Dy³⁺ Doped GdVO₄ Nanoparticles: Concentration and Annealing Effect. *J. Appl. Phys.* **2009**, *105*, 064303. [[CrossRef](#)]
61. Singh, N.S.; Ningthoujam, R.S.; Luwang, M.N.; Singh, S.D.; Vatsa, R.K. Luminescence, Lifetime and Quantum Yield Studies of YVO₄: Ln³⁺ (Ln³⁺ = Dy³⁺, Eu³⁺) Nanoparticles: Concentration and Annealing Effects. *Chem. Phys. Lett.* **2009**, *480*, 237–242. [[CrossRef](#)]
62. Yu, W.; Xu, W.; Song, H.; Zhang, S. Temperature-dependent Upconversion Luminescence and Dynamics of NaYF₄: Yb³⁺/Er³⁺ Nanocrystals: Influence of Particle Size and Crystalline Phase. *Dalton Trans.* **2014**, *43*, 6139–6147. [[CrossRef](#)]
63. Chihara, T.; Umezawa, M.; Miyata, K.; Sekiyama, S.; Hosokawa, N.; Okubo, K.; Kamimura, M.; Soga, K. Biological Deep Temperature Imaging with Fluorescence Lifetime of Rare-Earth-Doped Ceramics Particles in the Second NIR Biological Window. *Sci. Rep.* **2019**, *9*, 12806. [[CrossRef](#)] [[PubMed](#)]
64. Fu, Y.; Zhao, L.; Guo, Y.; Yu, H. Up-conversion Luminescence Lifetime Thermometry Based on the ¹G₄ State of Tm³⁺ Modulated by Cross Relaxation Processes. *Dalton Trans.* **2019**, *48*, 16034–16040. [[CrossRef](#)] [[PubMed](#)]
65. Savchuk, O.A.; Haro-González, P.; Carvajal, J.J.; Jaque, D.; Massons, J.; Aguiló, M.; Díaz, F. Er: Yb: NaY₂F₅O up-converting nanoparticles for sub-tissue fluorescence lifetime thermal sensing. *Nanoscale* **2014**, *6*, 9727–9733. [[CrossRef](#)]
66. Tan, M.; Li, F.; Cao, N.; Li, H.; Wang, X.; Zhang, C.; Jaque, D.; Chen, G. Accurate In Vivo Nanothermometry through NIR-II Lanthanide Luminescence Lifetime. *Small* **2020**, *16*, 2004118. [[CrossRef](#)]
67. Lu, K.; Yi, Y.; Xu, L.; Sun, X.; Liu, L.; Li, H. Temperature-Independent Lifetime and Thermometer Operated in a Biological Window of Upconverting NaErF₄ Nanocrystals. *Nanomaterials* **2020**, *10*, 24. [[CrossRef](#)]
68. Sun, Y.; Feng, W.; Yang, P.; Huang, C.; Li, F. The Biosafety of Lanthanide Upconversion Nanomaterials. *Chem. Soc. Rev.* **2015**, *44*, 1509–1525. [[CrossRef](#)]
69. Zhao, M.; Li, B.; Wu, Y.; He, H.; Zhu, X.; Zhang, H.; Dou, C.; Feng, L.; Fan, Y.; Zhang, F. A Tumor-Microenvironment-Responsive Lanthanide-Cyanine FRET Sensor for NIR-II Luminescence-Lifetime in Situ Imaging of Hepatocellular Carcinoma. *Adv. Mater.* **2020**, *32*, 2001172. [[CrossRef](#)]
70. Lin, Z.-Y.; Qu, Z.-b.; Chen, Z.-H.; Han, X.-Y.; Deng, L.-X.; Luo, Q.; Jin, Z.; Shi, G.; Zhang, M. The Marriage of Protein and Lanthanide: Unveiling a Time-Resolved Fluorescence Sensor Array Regulated by pH toward High-Throughput Assay of Metal Ions in Biofluids. *Anal. Chem.* **2019**, *91*, 11170–11177. [[CrossRef](#)]
71. Hanaoka, K.; Kikuchi, K.; Kobayashi, S.; Nagano, T. Time-Resolved Long-Lived Luminescence Imaging Method Employing Luminescent Lanthanide Probes with a New Microscopy System. *J. Am. Chem. Soc.* **2007**, *129*, 13502–13509. [[CrossRef](#)] [[PubMed](#)]
72. Cheng, S.; Shen, B.; Yuan, W.; Zhou, X.; Liu, Q.; Kong, M.; Shi, Y.; Yang, P.; Feng, W.; Li, F. Time-Gated Ratiometric Detection with the Same Working Wavelength to Minimize the Interferences from Photon Attenuation for Accurate In Vivo Detection. *ACS Central Sci.* **2019**, *5*, 299–307. [[CrossRef](#)]
73. Tian, L.; Ma, H.; Song, B.; Dai, Z.; Zheng, X.; Zhang, R.; Chen, K.; Yuan, J. Time-gated Luminescence Probe for Ratiometric and Luminescence Lifetime Detection of Hypochorous Acid in Lysosomes of Live Cells. *Talanta* **2020**, *212*, 120760. [[CrossRef](#)] [[PubMed](#)]
74. Song, B.; Ye, Z.; Yang, Y.; Ma, H.; Zheng, X.; Jin, D.; Yuan, J. Background-free in-vivo Imaging of Vitamin C Using Time-gateable Responsive Probe. *Sci. Rep.* **2015**, *5*, 14194. [[CrossRef](#)] [[PubMed](#)]
75. Lu, Y.; Lu, J.; Zhao, J.; Cusido, J.; Raymo, F.M.; Yuan, J.; Yang, S.; Leif, R.C.; Huo, Y.; Piper, J.A.; et al. On-the-fly Decoding Luminescence Lifetimes in the Microsecond Region for Lanthanide-encoded Suspension Arrays. *Nat. Commun.* **2014**, *5*, 3741. [[CrossRef](#)] [[PubMed](#)]

76. Mizukami, S.; Tonai, K.; Kaneko, M.; Kikuchi, K. Lanthanide-Based Protease Activity Sensors for Time-Resolved Fluorescence Measurements. *J. Am. Chem. Soc.* **2008**, *130*, 14376–14377. [[CrossRef](#)]
77. Mizukami, S.; Yamamoto, T.; Yoshimura, A.; Watanabe, S.; Kikuchi, K. Covalent Protein Labeling with a Lanthanide Complex and Its Application to Photoluminescence Lifetime-Based Multicolor Bioimaging. *Angew. Chem. Int. Ed.* **2011**, *50*, 8750–8752. [[CrossRef](#)]
78. Vuojola, J.; Syrjänpää, M.; Lamminmäki, U.; Soukka, T. Genetically Encoded Protease Substrate Based on Lanthanide-Binding Peptide for Time-Gated Fluorescence Detection. *Anal. Chem.* **2013**, *85*, 1367–1373. [[CrossRef](#)]
79. Tu, D.; Liu, L.; Ju, Q.; Liu, Y.; Zhu, H.; Li, R.; Chen, X. Time-Resolved FRET Biosensor Based on Amine-Functionalized Lanthanide-Doped NaYF₄ Nanocrystals. *Angew. Chem. Int. Ed.* **2011**, *50*, 6306–6310. [[CrossRef](#)]
80. Liu, Y.; Zhou, S.; Tu, D.; Chen, Z.; Huang, M.; Zhu, H.; Ma, E.; Chen, X. Amine-Functionalized Lanthanide-Doped Zirconia Nanoparticles: Optical Spectroscopy, Time-Resolved Fluorescence Resonance Energy Transfer Biodetection, and Targeted Imaging. *J. Am. Chem. Soc.* **2012**, *134*, 15083–15090. [[CrossRef](#)]
81. Zheng, W.; Zhou, S.; Chen, Z.; Hu, P.; Liu, Y.; Tu, D.; Zhu, H.; Li, R.; Huang, M.; Chen, X. Sub-10 nm Lanthanide-doped CaF₂ Nanoparticles for Time-resolved Luminescent Biodetection. *Angew. Chem. Int. Ed.* **2013**, *52*, 6671–6676. [[CrossRef](#)] [[PubMed](#)]
82. Jin, X.; Zeng, Q.; Zheng, J.; Xing, D.; Zhang, T. Aptamer-Functionalized Upconverting Nanoformulations for Light-Switching Cancer-Specific Recognition and in Situ Photodynamic-Chemo Sequential Theranostics. *ACS Appl. Mater. Inter.* **2021**, *13*, 9316–9328. [[CrossRef](#)]
83. Xu, Y.; Li, Q. Multiple Fluorescent Labeling of Silica Nanoparticles with Lanthanide Chelates for Highly Sensitive Time-Resolved Immunofluorometric Assays. *Clin. Chem.* **2007**, *53*, 1503–1510. [[CrossRef](#)] [[PubMed](#)]
84. Lu, J.; Martin, J.; Lu, Y.; Zhao, J.; Yuan, J.; Ostrowski, M.; Paulsen, I.; Piper, J.A.; Jin, D. Resolving Low-Expression Cell Surface Antigens by Time-Gated Orthogonal Scanning Automated Microscopy. *Anal. Chem.* **2012**, *84*, 9674–9678. [[CrossRef](#)] [[PubMed](#)]
85. Guo, H.; Song, X.; Lei, W.; He, C.; You, W.; Lin, Q.; Zhou, S.; Chen, X.; Chen, Z. Direct Detection of Circulating Tumor Cells in Whole Blood Using Time-Resolved Luminescent Lanthanide Nanoparticles. *Angew. Chem. Int. Ed.* **2019**, *58*, 12195–12199. [[CrossRef](#)]
86. Sayyadi, N.; Justiniano, I.; Connally, R.E.; Zhang, R.; Shi, B.; Kautto, L.; Everest-Dass, A.V.; Yuan, J.; Walsh, B.J.; Jin, D.; et al. Sensitive Time-Gated Immunoluminescence Detection of Prostate Cancer Cells Using a TEGylated Europium Ligand. *Anal. Chem.* **2016**, *88*, 9564–9571. [[CrossRef](#)]
87. Zhu, X.; Liu, X.; Zhang, H.; Zhao, M.; Pei, P.; Chen, Y.; Yang, Y.; Lu, L.; Yu, P.; Sun, C.; et al. High-Fidelity NIR-II Multiplexed Lifetime Bioimaging with Bright Double Interfaced Lanthanide Nanoparticles. *Angew. Chem. Int. Ed.* **2021**, *60*, 23545–23551. [[CrossRef](#)]
88. Siai, A.; Haro-González, P.; Horchani-Naifer, K.; Férid, M. La₂O₃: Tm, Yb, Er upconverting nano-oxides for sub-tissue lifetime thermal sensing. *Sens. Actuat. B-Chem.* **2016**, *234*, 541–548. [[CrossRef](#)]
89. Qiu, X.; Zhou, Q.; Zhu, X.; Wu, Z.; Feng, W.; Li, F. Ratiometric Upconversion Nanothermometry with Dual Emission at the Same Wavelength Decoded via a Time-resolved Technique. *Nat. Commun.* **2020**, *11*, 4. [[CrossRef](#)]
90. Liu, X.; Skripka, A.; Lai, Y.; Jiang, C.; Liu, J.; Vetrone, F.; Liang, J. Fast Wide-field Upconversion Luminescence Lifetime Thermometry Enabled by Single-shot Compressed Ultrahigh-speed Imaging. *Nat. Commun.* **2021**, *12*, 6401. [[CrossRef](#)]
91. Kong, M.; Gu, Y.; Chai, Y.; Ke, J.; Liu, Y.; Xu, X.; Li, Z.; Feng, W.; Li, F. Luminescence Interference-free Lifetime Nanothermometry Pinpoints In Vivo Temperature. *Sci. China Chem.* **2021**, *64*, 974–984. [[CrossRef](#)]
92. Estebanez, N.; Ferrera-González, J.; Cortez-Cevallos, I.A.; González-Béjar, M.; Pérez-Prieto, J. Lengthening the Lifetime of Common Emissive Probes to Microseconds by a Jigsaw-Like Construction of NIR-Responsive Nanohybrids. *Adv. Opt. Mater.* **2020**, *8*, 1902030. [[CrossRef](#)]
93. Cheng, S.; Liu, Q.; Zhou, X.; Gu, Y.; Yuan, W.; Feng, W.; Li, F. Reversible Ratiometric Probe Combined with the Time-Gated Method for Accurate In Vivo Gastrointestinal pH Sensing. *ACS Appl. Mater. Inter.* **2020**, *12*, 25557–25564. [[CrossRef](#)] [[PubMed](#)]
94. Ning, Y.; Cheng, S.; Wang, J.-X.; Liu, Y.-W.; Feng, W.; Li, F.; Zhang, J.-L. Fluorescence Lifetime Imaging of Upper Gastrointestinal pH In Vivo with a Lanthanide Based Near-infrared τ Probe. *Chem. Sci.* **2019**, *10*, 4227–4235. [[CrossRef](#)] [[PubMed](#)]
95. Ang, J.; Yoon, J.; Zhou, M.; Wei, H.-L.; Goh, Y.; Lok, K.; Liu, Y.; Li, Z.; Wang, H.; Su, Q.; et al. Deciphering Nanoparticle Trafficking into Glioblastomas Uncovers an Augmented Antitumor Effect of Metronomic Chemotherapy. *Adv. Mater.* **2022**, *34*, 2106194. [[CrossRef](#)]